**Title**
Relief of tumor hypoxia unleashes the tumoricidal potential of neutrophils.

**Permalink**
https://escholarship.org/uc/item/0qw7914r

**Journal**
The Journal of clinical investigation, 130(1)

**ISSN**
0021-9738

**Authors**
Mahiddine, Karim
Blaisdell, Adam
Ma, Stephany
et al.

**Publication Date**
2020

**DOI**
10.1172/jci130952

**Supplemental Material**
https://escholarship.org/uc/item/0qw7914r#supplemental

Peer reviewed

# Relief of tumor hypoxia unleashes the tumoricidal potential of neutrophils

Karim Mahiddine[1], Adam Blaisdell[2], Stephany Ma[1],

Amandine Créquer-Grandhomme[2], Clifford A. Lowell[1, 3, 4], and Adrian Erlebacher[1, 3-5]

[1]Department of Laboratory Medicine, University of California San Francisco, San Francisco, CA, 94143, USA

[2]Department of Pathology, NYU School of Medicine, New York, NY, 10016, USA

[3]Biomedical Sciences Program, University of California San Francisco, San Francisco, CA, 94143, USA

[4]ImmunoX Program, University of California San Francisco, San Francisco, CA, 94143, USA

[5]Center for Reproductive Sciences, University of California San Francisco, San Francisco, CA, 94143, USA

Address for correspondence:
Adrian Erlebacher
Department of Laboratory Medicine
University of California San Francisco
513 Parnassus Ave.
Medical Sciences, S-1057B
San Francisco, CA 94143-0451
Tel: (415) 502-3583
adrian.erlebacher@ucsf.edu

**ABSTRACT**

Polymorphonuclear neutrophils (PMNs) are increasingly recognized to influence solid tumor development, but why their effects are so context-dependent and even frequently divergent remains poorly understood. Using an autochthonous mouse model of uterine cancer and the administration of respiratory hyperoxia as a means to improve tumor oxygenation, we provide in vivo evidence that hypoxia is a potent determinant of tumor-associated PMN phenotypes and direct PMN-tumor cell interactions. Upon relief of tumor hypoxia, PMNs were recruited less intensely to the tumor-bearing uterus but the recruited cells much more effectively killed tumor cells, an activity our data moreover suggested was mediated via their production of NADPH oxidase-derived reactive oxygen species and MMP-9. Simultaneously, their ability to promote tumor cell proliferation, which appeared mediated via their production of neutrophil elastase, was rendered less effective. Relieving tumor hypoxia thus greatly improved net PMN-dependent tumor control, leading to a massive reduction in tumor burden. Remarkably, this outcome was T cell-independent. Together, these findings identify key hypoxia-regulated molecular mechanisms through which PMNs directly induce tumor cell death and proliferation in vivo and suggest that the contrasting properties of PMNs in different tumor settings may in part reflect the effects of hypoxia on direct PMN-tumor cell interactions.

**INTRODUCTION**

Polymorphonuclear neutrophils (PMNs) are thought to play an important, if controversial, role in cancer (reviewed in (1, 2)). Elevated blood PMN numbers are associated with poor prognosis in many human cancers, and results from mouse models have suggested that this association variously reflects the ability of PMNs to promote tumor cell proliferation, tumor angiogenesis, metastasis, and the establishment of immunosuppressive tumor microenvironments. Although less well understood, PMNs may also oppose tumorigenesis under certain circumstances (reviewed in (3)). For example, PMNs are thought to inhibit the early stages of lung cancer by fostering anti-tumor T cell responses (4). A second example comes from our work on endometrioid endometrial adenocarcinoma, the most prevalent gynecological malignancy. Using a mouse model of this cancer, we were able to demonstrate PMN-mediated inhibition of tumor growth that, in this case, occurred in a T cell-independent fashion (5). Our analysis of The Cancer Genome Atlas (TCGA) database moreover revealed that patients with endometrioid endometrial cancer survived longer if their primary tumors displayed high PMN transcriptional signatures. Other human cancers, including invasive ductal carcinoma of the breast, low grade glioma, and colorectal cancer, showed similar positive correlations, even though PMN signatures predicted poor patient survival when all solid tumor types were considered in aggregate (5). Although controversial, several immunohistochemical studies have also uncovered a correlation between the presence of tumor-associated PMNs and improved patient outcomes in colorectal cancer, and a similar correlation might exist with certain types of lung cancers (2).

The most likely explanation for these divergent associations is that PMNs assume different phenotypes within different tumor microenvironments (1, 2, 6). For example, early studies suggested that tumor-associated PMNs can assume either a pro-inflammatory "N1" phenotype or an immunosuppressive, tumor-promoting "N2" phenotype (7). In recent work, it has been found that a SiglecF$^{hi}$ PMN subset promotes tumor growth in a mouse model of lung cancer (8), and that PMNs expressing class II HLA molecules accumulate in human lung cancer specimens (9). In these and other cases, however, the key characteristics of the tumor microenvironment that determine resident PMN phenotypes remain unclear. Elucidating the contributions of PMNs to tumorigenesis is further complicated by the likelihood that PMN-derived products, which are frequently cytotoxic for tumor cells in vitro (3, 10, 11), may each have their own complex and context-dependent effects in vivo. For example, neutrophil elastase (NE) and MMP-9 are both able to cause epithelial cell death as evidenced by their contributions to epidermal destruction in bullous pemphigoid disease (12, 13), but NE can also

directly promote tumor cell proliferation in lung cancer (14), while MMP-9 promotes tumor angiogenesis (15). Similarly, PMN-derived reactive oxygen species (ROS) contribute to epithelial damage in inflammatory bowel disease (16) and can restrain malignant processes at pulmonary metastatic sites (17), but are also thought to contribute to the generation of immunosuppressive tumor microenvironments (18).

Hypoxia, a universal if variable feature of all solid tumors, is well known to modulate PMN phenotypes (reviewed in (19, 20)). When studied outside the context of cancer, hypoxia has been shown to augment PMN lifespan (21) and to promote PMN degranulation and protease release (22), effects that are likely in part mediated via activation of the hypoxia sensing transcription factors HIF-$1\alpha$ and HIF-$2\alpha$ (21, 23, 24). On the other hand, hypoxia reduces the capacity of PMNs to produce ROS (25). Although less well studied, hypoxia in the tumor microenvironment is thought to promote the recruitment and T cell suppressive activity of polymorphonuclear (i.e. granulocytic) myeloid derived suppressor cells (PMN-MDSCs) (26), cells considered to be the product of a deranged PMN differentiation program (1, 2, 27). Importantly, much of the work on the effects of hypoxia on PMNs and PMN-MDSCs has been performed on isolated cells in vitro or through the use of mice with myeloid cell-targeted genetic disruptions of HIF pathway components (20-26, 28, 29). Since altered $O_2$ levels within tissues are expected to have both direct and indirect effects on any given cell type, however, the net effect of hypoxia on PMNs within the overall context of the tumor microenvironment remains incompletely understood. In addition to being fundamental to our understanding of how PMNs contribute to tumor development, this question has gained even greater salience given the emerging possibility that hypoxia relief could be used an adjunct modality in cancer immunotherapy (30, 31). Indeed, recent work in mice has suggested that therapeutic relief of tumor hypoxia is able to augment anti-tumor T cell responses both following immune checkpoint blockade as well as when applied as the sole manipulation (32, 33). In the context of checkpoint blockade, the effect has in turn been linked to less MDSC accumulation and less T cell-suppressive MDSC phenotypes (33). Whether altered $O_2$ levels might also affect the ability of PMNs to act as direct anti-tumor effectors, however, has not yet been addressed.

Here, we provide in vivo evidence that one of the aggregate, top-down effects of tumor hypoxia in vivo is to limit the ability of PMNs to directly combat tumorigenesis, independently of T cells. Moreover, we identify specific PMN effector functions through which hypoxia exerts its effects in vivo, namely the induction of tumor cell death by ROS and MMP-9, which is inhibited by hypoxia,

and the induction of tumor cell proliferation by NE, which is promoted by hypoxia. This work employs use of respiratory hyperoxia as a means to directly manipulate tumor hypoxia and builds upon our aforementioned mouse model of endometrioid endometrial adenocarcinoma. This model is generated by expressing Cre recombinase from the progesterone receptor (PR) promoter to drive uterus-specific deletion of *Pten*, the tumor suppressor gene whose loss drives this disease in humans (5, 34, 35). In such PRPL (<u>PR</u>-Cre [*Pgr*-Cre$^{+/-}$] <u>*Pten*</u>$^{lox/lox}$) mice, uterine epithelial hyperplasia is evident by 2 wks of age, and progresses synchronously throughout the uterus to carcinoma in situ by ~4 wks of age. Previously, we showed that PMNs massively infiltrate PRPL tumors, become activated via a MyD88-dependent pathway, and then oppose tumor growth as evidenced in part by the markedly increased tumor burden apparent when we depleted the mice of PMNs, either via antibody-mediated neutralization of the growth factor G-CSF, or via genetic disruption of *Csf3r*, which encodes its receptor (5). Accordingly, the survival of PRPL-*Csf3r*$^{-/-}$ mice was also shorter than that of PRPL mice. Through the analysis of 4-wk old mice, we moreover found the anti-tumor effects of PMNs to be lymphocyte-independent, as tumor burden was unaffected when the mice were additionally rendered either *Rag2*- or *Rag2*/*Il2rg*-deficient. Instead, these effects were attributable to an ability of PMNs to induce the detachment of live PRPL tumor cells from their basement membrane, leading to their death secondarily within the uterine lumen. Importantly, this previous study also linked tumor-associated PMN trafficking to tumor hypoxia, since PMNs began infiltrating PRPL tumors when they first became hypoxic and then aggregated in areas of severe tumor hypoxia. Our analysis of the TCGA database moreover supported an association between hypoxia and PMN infiltration in human endometrial cancer (5). We now show that hypoxia indeed promotes PMN recruitment to PRPL tumors, but then alters their phenotype in situ to limit their ability to directly inhibit tumor growth. Upon therapeutic relief of tumor hypoxia, PMN-dependent tumor control was greatly enhanced despite a reduction in PMN infiltration, and this occurred in a T cell-independent fashion. These findings bear upon our understanding of the contribution of PMNs towards tumorigenesis and suggest that PMNs might play a greater role than previously anticipated as direct anti-tumor effectors in the context of therapeutic hypoxia relief.

**RESULTS**

**Relief of tumor hypoxia reduces PMN infiltration into PRPL tumors but improves PMN-dependent tumor control.**

To directly assess the role of hypoxia in PMN-tumor cell interactions, we housed PRPL mice in a 60% $O_2$ environmental chamber. This high level of respiratory $O_2$ exposure is thought to increase oxygen delivery to tissues by increasing the partial pressure of $O_2$ dissolved in arterial blood (36), and was previously shown to be able to improve the oxygenation of the non-tumor-bearing mouse uterus (37). We chose to house the mice in the chamber starting on postnatal day (P) 18, because this time point corresponded to when the tumors first started accumulating PMNs and showing signs of hypoxia (5), and to sacrifice them 10 days later on P28, because P28 was the primary terminal end point we employed in our previous study (5). As controls, 'normoxia' mice were maintained at ambient $O_2$ for the same time period. Consistent with results from other species (38), 10 days of hyperoxia exposure did not induce lung inflammation (Supplemental Figure 1A-C).

Strikingly, hyperoxia housing reduced the uterine tissue densities (cells/mg tissue) of PMNs by ~60% (Figure 1A, Supplemental Figure 1D), without affecting the densities of other uterine leukocyte species (Supplemental Figure 1E). Conversely, blood PMNs concentrations were modestly increased following hyperoxia exposure (Figure 1B), but this could not be attributed to an increase in immature PMN release from the bone marrow, since blood (as well as uterine) PMNs showed the same Ly6G$^{hi}$ fully mature (39) phenotype under both hyperoxia and normoxia housing conditions (Supplemental Figure 1F-H). Rather, we found that hyperoxia housing decreased tumor cell production of CXCL5, a potent PMN chemoattractant and inflammatory marker (Figure 1C, Supplemental Figure 2A-B). Importantly, our previous study employed PRPL mice deficient in the CXCL1/2/5 receptor CXCR2 to demonstrate an absolute requirement for CXCR2 ligands in recruiting PMNs from the blood to the PRPL uterus, while our decision to focus on CXCL5 was motivated by our prior demonstration that CXCL5 was the CXCR2 ligand most highly induced in PRPL uteri following the onset of tumor hypoxia at ~3 wks of age (5), as well as the existence of CXCL5-specific antibodies suitable for immunofluorescence that enabled us to determine expression levels on a per tumor cell basis. Thus, our new observations taken together not only demonstrated that hyperoxia housing could decrease uterine PMN densities in PRPL mice, but also suggested that a major underlying mechanism was reduced PMN recruitment from the blood secondary at least in part to decreased CXCL5 production by

PRPL tumor cells. The reduction in PMN recruitment in turn likely caused a backup of mature cells in the blood.

Importantly, PMNs themselves can cause tissue hypoxia (40) and are major contributors to tumor inflammation (1), thus creating the potential for feed-forward loops. Accordingly, we also applied respiratory hyperoxia to PRPL-*Csf3r*$^{-/-}$ mice, which are markedly deficient in uterine PMNs (ref. (5); see also Figure 3A-B), in order to identify which of its intrauterine effects were PMN-independent. As with PRPL mice, the tumor cells of hyperoxia-housed PRPL-*Csf3r*$^{-/-}$ mice expressed less CXCL5 than their normoxia counterparts (Figure 1C, Supplemental Figure 2C-D). Moreover, they showed much less nuclear accumulation of HIF-1α, a direct marker of hypoxia (Figure 1D-F), as well as less nuclear accumulation of phospho-STAT3, which we found was in turn required for CXCL5 induction (Figure 1D, Supplemental Figure 2E-F, Supplemental Figure 3). In contrast, their level of nuclear NF-κB p65, another inflammatory marker, remained unchanged (Figure 1D, Supplemental Figure 2G-H). Together these results suggested that respiratory hyperoxia improved PRPL tumor oxygenation in a PMN-independent fashion and that the ensuing relief of tumor hypoxia had several PMN-independent effects on PRPL tumor cells, including decreased CXCL5 expression that in turn reduced PMN recruitment.

Given these results and our prior evidence that PMNs oppose PRPL tumor growth (5), we were surprised to find that the tumor burden of PRPL mice housed in hyperoxia conditions – calculated from measurements of uterine weights and histological assessments of how much each uterus was comprised of tumor cells (Supplemental Figure 4A-B) – was 2.3-fold *lower* than the tumor burden of PRPL mice housed in normoxia conditions (Fig. 2A, 2C-D). The reduction in tumor burden was still PMN-dependent, however, since hyperoxia housing did not alter the high tumor burden of PRPL-*Csf3r*$^{-/-}$ mice (Figure 2B, 2F-G, Supplemental Figure 4A-B). Importantly, these divergent outcomes were not a consequence of differences in tumor burdens between PRPL and PRPL-*Csf3r*$^{-/-}$ mice at the time we commenced hyperoxia exposure on P18; rather, tumor burdens on P18 were equivalent (Supplemental Figure 4D), consistent with this time point marking the initial onset of tumor hypoxia and PMN infiltration. Moreover, the reduction in tumor burden in PRPL mice following hyperoxia exposure was T cell-independent since it was also apparent when the mice were concurrently T cell-depleted (Figure 2A, 2E, Supplemental Figure 4A-C), consistent with our aforementioned observation that 4-wk old PRPL, PRPL-*Rag2*$^{-/-}$, and PRPL-*Rag2*$^{-/-}$ *Il2rg*$^{-/-}$ mice all have similar tumor burdens when housed under normoxia conditions (5). Together, these data suggested that hypoxia had a net

7

inhibitory effect on the capacity of PMNs to directly restrain tumor growth, despite its promotion of PMN recruitment.

**Tumor hypoxia influences both PMN-induced tumor cell death and PMN-induced tumor cell proliferation.**

Previously, by comparing normoxia-housed PRPL to PRPL-*Csf3r*$^{-/-}$ mice, we had found that PMNs induced both tumor cell death and tumor cell proliferation (5). The cause of cell death was not the direct induction of tumor cell apoptosis but rather a process we referred to as tumor cell 'sloughing' in which PMNs caused live tumor cells to detach from their basement membrane, leaving behind prominent segments of endometrial stromal surfaces 'denuded' of their overlying epithelium and thus directly contacting the uterine lumen (e.g. see Figure 3A-B). Consistent with such a process, the tumor cells in PRPL mice comprising epithelial sheets still attached to the endometrial stroma had lost their basolateral polarization of integrin α6β4, an integrin that is critical for epithelial cell adhesion to basement membranes. This polarization was still evident in PRPL-*Csf3r*$^{-/-}$ mice (Figure 3C-D shows representative staining for the α6 subunit). Following detachment, tumor cell debris admixed with PMNs could be seen within the uterine lumen, with the cells presumably dying by either apoptosis or necrosis. In this prior report, we interpreted the PMN-dependent increase in tumor cell proliferation as a wound-healing response induced secondary to the denudation of the endometrial stroma.

Thus, to gain greater insight into how hypoxia limited the capacity of PMNs to restrain PRPL tumorigenesis, we determined how hyperoxia housing respectively affected tumor cell death and proliferation. Strikingly, hyperoxia housing increased the amount of sloughed tumor and denuded endometrial surface, while it decreased the amount of tumor epithelium with basolateral α6 polarization as well as the rate of tumor cell proliferation, as measured by phospho-histone H3 (pH3) immunostaining to identify mitotic cells (Figure 3E-J, Supplemental Figure 5A-B). These changes were not apparent in PRPL-*Csf3r*$^{-/-}$ mice, indicating that they were PMN-dependent (Figure 3G-J, 2F-G, Supplemental Fig 5C-D). Moreover, the changes were unaffected by T cell depletion (Supplemental Figure 4E-H), in accord with T cells not playing a role in the hyperoxia-induced reduction in PRPL tumor burden (Figure 2A), nor were they associated with a change in tumor cell apoptosis among those cells still attached to their basement membrane, as revealed by an immunofluorescence analysis of cleaved caspase-3 expression (Supplemental Figure 6A-C). Collectively, these results suggested that improved tumor oxygenation augmented PMN-dependent tumor control via a two-pronged effect:

increased tumor cell death (secondary to increased tumor cell sloughing) and decreased tumor cell proliferation. Moreover, they indicated that the higher rate of tumor cell proliferation in PRPL versus PRPL-*Csf3r*^{-/-} mice under normoxia conditions actually reflected a direct pro-proliferative effect of PMNs rather than a wound-healing response, since hyperoxia housing *decreased* tumor cell proliferation while it simultaneously *increased* tumor cell death.

**Individual PMN products have divergent effects on PRPL tumorigenesis, and divergently manifest these effects with improved tumor oxygenation.**

Next, we noted that the hyperoxia-induced reduction in tumor burden was not merely due to greater PMN accumulation within the tumor epithelium, since uterine PMNs in hyperoxia-housed PRPL mice instead assumed a more stromal distribution (Supplemental Figure 6D-F). Thus, to identify the hyperoxia-regulated mechanisms of PMN-induced tumor cell death (i.e. sloughing) and proliferation, we evaluated PRPL mice with genetic lesions preventing generation of PMN products with previously linked to cancer and basement membrane degradation, namely PRPL-*Elane*^{-/-} mice deficient in neutrophil elastase (NE), PRPL-*Mmp9*^{-/-} mice deficient in MMP-9, and PRPL-*Cybb*^{-/-} mice deficient in the gp91[phox] subunit of the NADPH oxidase complex expressed by PMNs (NOX2) and used by PMNs to produce high levels of ROS following activation (3, 12, 14). As with PRPL-*Csf3r*^{-/-} mice, these three additional mouse strains all showed the same tumor burdens as PRPL mice at the start of hyperoxia exposure on P18 (Supplemental Figure 6G). Interpretively, we considered the amount of denuded endometrial surface to be a positive function of the level of tumor cell sloughing, since tumor cell sloughing generates these surfaces, but a negative function of tumor cell proliferation, since proliferation-induced re-epithelialization would be expected to promote their disappearance.

Most straightforwardly, exposure of PRPL-*Elane*^{-/-}, PRPL-*Cybb*^{-/-}, and PRPL-*Mmp9*^{-/-} mice to respiratory hyperoxia had no effect on their respective tumor burdens, thus indicating that NE, NOX2-derived ROS, and MMP-9 were all involved in the influence of hypoxia over net tumor growth (Figure 4A-I). However, whereas the tumor burdens of normoxia-housed PRPL-*Cybb*^{-/-} and PRPL-*Mmp9*^{-/-} mice were similar to PRPL mice, the tumor burdens of PRPL-*Elane*^{-/-} mice were greatly reduced. This reduction could be attributed to a low level of tumor cell proliferation, which was evident under both normoxia and hyperoxia conditions and was moreover unaffected by hyperoxia housing (Figure 4J). Together, these results suggested that NE fostered tumor cell proliferation, similar to its previously documented effect in lung cancer (14), and that relief from tumor hypoxia decreased tumor cell

proliferation in PRPL mice in part by attenuating this influence. Consistent with this possibility, hyperoxia-induced tumor cell sloughing appeared NE-independent, since hyperoxia housing, despite having no effect on tumor proliferation in PRPL-*Elane*^{-/-} mice, increased their % denuded surface and decreased their α6 basolateral staining (Figure 4K, 4L, and Supplemental Figure 5E-F). On the other hand, hyperoxia housing did not increase the amount of sloughed tumor cells in PRPL-*Elane*^{-/-} mice (Figure 4M), as might have been expected, but we considered it unlikely that changes in sloughing would be detectable when tumor burden was so low and potentially only highly adherent remained attached to the endometrial stromal surface. A similar consideration likely explained why hyperoxia housing did not further decrease tumor burden in PRPL-*Elane*^{-/-} mice (Figure 4C, 4D, 4I).

We next noted that tumor cell proliferation in PRPL-*Cybb*^{-/-} mice was also low, like in PRPL-*Elane*^{-/-} mice, and was similarly unaffected by hyperoxia housing (Figure 4J). This suggested that NOX2-derived ROS also promoted PRPL tumor cell proliferation and that this influence waned when the tumor was rendered less hypoxic. However, since the tumor burdens of normoxia-housed PRPL-*Cybb*^{-/-} mice were similar to PRPL mice, their low tumor cell proliferation rate must have been canceled out by a concomitant reduction in tumor cell sloughing. Consistent with this possibility, α6 basolateral staining was dramatically increased in normoxia-housed PRPL-*Cybb*^{-/-} (versus PRPL mice; Figure 4L, Supplemental Fig 5A, 5G). Moreover, hyperoxia housing only mildly affected this high level of staining and had no effect on % denuded surface or amount of intraluminal debris (Figure 4K-M, Supplemental Figure 5G, 5H). Similarly, PRPL-*Mmp9*^{-/-} mice showed no change in % denuded surface, amount of intraluminal debris, or α6 basolateral staining following hyperoxia housing, with their α6 basolateral staining under normoxia housing conditions marginally increased over PRPL mice ($P$=0.078) (Figure 4K-M, Supplemental Figure 5A, 5I-J). Together, these observations suggested a dual requirement for NOX2-derived ROS and MMP-9 in tumor cell killing, particularly under conditions of improved tumor oxygenation. Tumor cell proliferation in PRPL-*Mmp9*^{-/-} mice remained similar to PRPL mice and sensitive to respiratory hyperoxia, suggesting that it was not controlled by MMP-9 in a major way (Figure 4J). Of interest, NE deficiency reduced PMN tissue densities in PRPL tumors, while NOX2 and MMP-9 deficiencies abrogated the response of these densities to respiratory hyperoxia (Figure 4N). Most likely, these latter findings reflected the respective impact of the *Elane*, *Cybb* and *Mmp9* mutations on tumor burden and thus intrinsic levels of tumor hypoxia, combined with the aforementioned ability of PMNs to promote hypoxia and inflammation and thus their own recruitment in feed-forward fashion.

These mouse mutants also provided insight into how hyperoxia housing and tumor-associated PMNs controlled the advent of *severe* tumor hypoxia, as revealed through use of pimonidazole, a hypoxia-sensing reagent that becomes reactive when local tissue $O_2$ levels fall below 1.3% (41). This was not a straightforward issue since the percentage of pimonidazole[+] tumor area in PRPL-*Csf3r*^{-/-} mice was not reduced when the mice were housed in hyperoxia conditions (Supplemental Figure 7A, 7J-K), despite the tumor cells showing dramatically reduced nuclear HIF-1α staining, as described above (Figure 1D-F). These observations suggested a disconnect between the processes that were inducing the moderate levels of hypoxia (i.e. $O_2$ below ~6%) sufficient to induce HIF-1α activation (42), and the processes that were inducing severe hypoxia, as revealed by the pimonidazole reaction. As discussed further below, however, we noted that the percentages of pimonidazole^{+} tumor cells across all mouse groups analyzed (Supplemental Figure 7) were elevated only when the data above suggested high tumor cell exposure to NE, and not in cases of high tumor cell proliferation, high ROS production by PMNs, or low levels of tumor cell killing.

**Hypoxia alters the transcriptional signature of tumor-associated PMNs.**

To gain greater insight into how hypoxia altered the functionality of tumor-associated PMNs, we performed RNA-Seq on PMNs sorted from the uteri of PRPL mice housed in hyperoxia and normoxia conditions. Of the 423 protein coding genes were differentially expressed (Figure 5A and Supplemental Table 1), some of the more interesting became clear when we visualized differential expression in terms of absolute changes in normalized read counts (Figure 5B). One gene upregulated in PMNs from hyperoxia uteri was *Cybb*, consistent with prior results with mouse PMN-MDSCs (26) and suggestive of greater ROS production. These cells also expressed higher levels of *Mmp2* and *Mmp14*, which encode key activators of MMP-9 (43). *Mmp9* itself was highly expressed by tumor-associated PMNs, as expected (5), but not differentially expressed (data not shown). Indeed, gelatin zymography performed on PRPL uterine extracts revealed similar total MMP-9 levels (active plus inactive forms) when the mice were housed in hyperoxia conditions, but a greater amount of the active form (Figure 5C, 5F). Since hyperoxia conditions reduced PMN densities by ~60% (Figure 1A), this increase likely underestimates the amount of active MMP-9 generated by PMNs on a per cell basis. Irrespective of housing condition, uterine MMP-9 levels in PRPL mice were much higher than in PRPL-*Csf3r*^{-/-} mice (Figure 5C), indicating that PMNs were a major source of MMP-9 in PRPL tumors, in accord with our prior immunofluorescence analysis (5). Moreover, hyperoxia housing did

not increase MMP-9 activation in the uteri of PRPL-*Csf3r*^{-/-} mice (Figure 5D). This observation indicated that the elevation in MMP-9 activity seen in the uteri of hyperoxia-housed PRPL mice involved the PMN-dependent component of its production and activation, and was consistent with the hyperoxia housing-induced increase in the cells' expression of *Mmp2* and *Mmp14*.

Given the recent description of HLA class II-expressing PMNs in human cancer (9), we also noted the upregulated expression of genes related to peptide-MHC class II complex generation and co-stimulation, including *Cd74, Ciita, H2-Ab1, H2-Aa, H2-Eb1,* and *Cd40* (Figure 5A-B). With respect to downregulated genes, *Siglecf* stood out (Figure 5B) given the recent identification of SiglecF as a marker of tumor-promoting PMNs in lung cancer (8). *Elane* transcripts were undetectable under both normoxia and hyperoxia conditions, consistent with this gene's transcription during granulopoiesis (44), however casein zymograms revealed decreased intrauterine NE activity following hyperoxia housing (Figure 5E, 5G). These zymograms also revealed a total lack of NE activity in the uteri of PRPL-*Csf3r*^{-/-} mice, indicating that the source of this enzyme was exclusively PMNs. Of interest, the transcriptional changes in uterine PMNs isolated from hyperoxia- versus normoxia-housed PRPL mice did not bear an obvious relationship to the differences between N1 and N2 PMNs (45). Moreover, only a limited number of the differentially expressed genes we identified were present in a recent comparison between immunosuppressive PMN-MDSCs from cancer patients and their normal PMN counterparts (46), and these genes (e.g. *Cpvl*, *S100a10*, *Ahnak*, and genes encoding MHC II molecules) were all expressed at respectively higher levels in both PMN-MDSCs and hyperoxia-exposed PMNs, despite the apparently contrasting biological properties of these cell types.

**PMNs exist as malleable, hypoxia-regulated subpopulations in the tumor microenvironment.**

Capitalizing on these data, we performed flow cytometry on disaggregated uterine tissues to further determine how hypoxia altered PMN phenotypes within the tumor microenvironment. As a point of comparison, we also assessed PMNs recruited to non-tumor-bearing uteri. Recruitment was accomplished by injecting LPS 24 h prior to sacrifice into the uterine lumen of 4 wk old phenotypically wild-type "PL" mice bearing floxed alleles of *Pten* but no *Pgr*-Cre transgene. Remarkably, LPS injection induced the sloughing of the uterine epithelium, and this was primarily due to the recruited PMNs since it was much less apparent in LPS-injected PL-*Csf3r*^{-/-} mice (Figure 6A-C, Supplemental Figure 8A). For both PRPL and LPS-injected PL mice, uterine but not blood PMNs divided into CD11b^{lo} versus CD11b^{hi} subsets at a ~80/20% relative proportion that was unaffected by

hyperoxia housing (Figure 6D, Supplemental Figure 8B). Both subsets moreover contained cells that were producing ROS as well as cells expressing SiglecF. Strikingly, hyperoxia housing altered the expression of these two markers, but this effect was evident only in PRPL mice and was much more apparent with the CD11b$^{lo}$ subset (Figure 6E-G, Supplemental Figure 8C-E). For this subset, hyperoxia housing reduced the proportion of ROS$^{-}$ SiglecF$^{+}$ cells, increased the proportion of ROS$^{+}$ SiglecF$^{-}$ cells, and reduced SiglecF expression levels on ROS$^{+}$ SiglecF$^{+}$ double positive cells. CD11b$^{hi}$ uterine PMNs, by contrast, showed only statistically insignificant changes (albeit with directionally parallel trends) and were much more ROS$^{+}$ SiglecF$^{+}$ double positive to begin with in PRPL mice (Supplemental Figure 8C-E). Blood PMNs showed no ROS production and their expression of SiglecF, which was detectable on ~20% of the cells in both PRPL and LPS-injected PL mice, was unchanged by hyperoxia housing (Supplemental Figure 8F-G).

These observations were consistent with the *Cybb* and *Siglecf* expression changes detected by RNA-Seq. We also found that hyperoxia housing increased the level of MHCII expression by tumor-associated PMNs, also consistent with the RNA-Seq analysis. In this case, however, it was the CD11b$^{hi}$ and not CD11b$^{lo}$ subset that was affected, but similar to our results with ROS production and SiglecF expression, the shift was not apparent in blood PMNs nor in PMNs recruited to the uterus by LPS (Supplemental Figure 9A-D). Together, these results suggested that the phenotype of tumor-associated PMNs remains malleable and that hyperoxia housing altered this phenotype at least in part by relieving tumor hypoxia and not by having some kind of de novo and potentially artifactual or systemic effect on PMNs. Consistent with this possibility, hyperoxia housing did not augment epithelial sloughing in LPS-injected PL mice (Supplemental Figure 8A). Importantly, we cannot formally rule out the possibility that hyperoxia housing had additional effects on PMNs prior to their extravasation into the tumor bearing uterus, however our observation that blood PMNs in PRPL mice had a uniformly Ly6G$^{hi}$ surface phenotype following both normoxia and hyperoxia housing (Supplemental Figure 1F-H) argues against hyperoxia exposure inducing emergency granulopoiesis and thus a shift towards an immature PMN phenotype. On the other hand, and consistent with an effect of the tumor per se on granulopoiesis, PMN frequencies in the blood are mildly elevated in the blood of 4-wk old PRPL compared to PL mice (5), while ~5% of blood PMNs in PRPL but not PL mice expressed MHCII (Supplemental Figure 9C-D).

Of note, levels of SiglecF expression by PMNs within PRPL and LPS-injected PL uteri barely reached those of eosinophils in the same specimens (Supplemental Figure 9E), thus distinguishing

SiglecF$^+$ PMNs in 4-wk PRPL tumors from lung cancer-associated PMNs, whose SiglecF expression levels are similar to that of eosinophils (8). Provocatively, however, SiglecF expression by uterine PMNs was much more pronounced when the cells were isolated from 12-wk old PRPL mice, thus suggesting an effect of tumor stage upon PMN phenotypes (Supplemental Figure 9F-G).

**PMNs, employing both NOX2 and mitochondria, constitute the vast majority of ROS-producing cells in PRPL tumors, but hypoxia only regulates ROS production by NOX2.**

Given that the two PMN subsets in PRPL tumors showed different behaviors with respect to ROS production, we next determined the extent to which these two subsets produced ROS via NOX2 and thus might contribute towards the NOX2-dependent tumor cell killing we documented using PRPL-*Cybb*$^{-/-}$ mice. As expected from the above flow analysis, hyperoxia housing increased ROS production by CD11b$^{lo}$ PMNs (now viewing the cells in aggregate independent of SiglecF expression levels). This increase was dependent upon NOX2 as it was not apparent in CD11b$^{lo}$ PMNs isolated from the uteri of hyperoxia-housed PRPL-*Cybb*$^{-/-}$ mice (Figure 7A). Unexpectedly, however, ROS production by CD11b$^{lo}$ PMNs from PRPL-*Cybb*$^{-/-}$ mice was still quite substantial (~40% positive cells) and similar to that of CD11b$^{lo}$ PMNs from PRPL mice housed under normoxia conditions (Figure 7A). A similar pattern was evident with CD11b$^{hi}$ PMNs (which in general produced more ROS than their CD11b$^{lo}$ counterparts), although their hyperoxia-induced increase in ROS production, following their isolation from PRPL mice, was more modest in terms of fold-induction (and did not reach statistical significance; Figure 7B). NOX2-dependent ROS production following hyperoxia housing was also evident when all PMNs were considered together (Figure 7C). Importantly, ROS production via mitochondrial respiration is known to be elevated in PMNs isolated from human patients with *Cybb* deficiencies (47), thus precluding rigorous interpretation of these data with respect to the relative contributions of NOX2 versus mitochondrial respiration to ROS production by tumor-associated PMNs in PRPL tumors, however they are consistent with the possibility that mitochondrial respiration and not NOX2 is the dominant source of PMN-derived ROS in the PRPL tumor microenvironment under normoxia housing conditions. Moreover, we found that PMNs constitute the vast majority (~90%) of ROS producing cells in the PRPL tumor microenvironment under both normoxia and hyperoxia housing conditions, with the amount of ROS produced by PMNs on a per cell basis also greatly exceeding all other cell types (Figure 7D-E). Together, these data suggest that mitochondrial respiration by PMNs is the major source of ROS in the PRPL tumor microenvironment, particularly

when the tumor is allowed to remain hypoxic, and that stimulation of NOX2 activity in PMNs upon relief of tumor hypoxia generates the ROS that promotes tumor cell sloughing.

**DISCUSSION**

A key question that arises when considering the role of PMNs in tumorigenesis is why their effects appear so context-dependent. Here, using an autochthonous mouse model of endometrial cancer and the administration of respiratory hyperoxia to improve tumor oxygenation, we provide in vivo evidence that hypoxia exerts a powerful but complex influence over tumor-associated PMN behavior and phenotypes. In the most general terms, we found that hypoxia promoted PMN recruitment to the tumor-bearing uterus but then prevented the cells from reaching their maximal tumor-combatting potential. These divergent effects, however, were unequally balanced, as the reduction in PMN recruitment to the tumor-bearing uterus achieved via the administration of respiratory hyperoxia was more than compensated for by the augmented ability of the recruited cells to oppose tumor growth. Thus, relieving tumor hypoxia greatly improved net PMN-dependent tumor control and caused a massive reduction in tumor burden. Importantly, improved tumor control in this tumor model was completely T cell-independent and instead reflected alterations in the direct interactions between PMNs and tumor cells. Given the variable presence of hypoxia in different tumor settings, these data thus suggest one way that the context-dependent effects of PMNs in cancer might be understood. Importantly, these hypoxia-regulated interactions may have less relevance to non-epithelial cancers given the basement membrane-dependent killing mechanism we describe here. Moreover, with the increasingly recognized possibility that hypoxia can augment the ability of PMN/PMN-MDSCs to suppress T cells (26, 33), the ultimate link between hypoxia-regulated PMNs and clinical outcome is likely to be explained through a combination of T cell-dependent and T cell-independent pathways. Indeed, our ability to gather evidence in support of direct hypoxia-regulated PMN-tumor cell interactions may have been facilitated by the fact that PRPL tumors are not controlled by T cells at their early stage of development (5).

Our results suggested that hypoxia promotes PMN recruitment to 4 wk PRPL lesions at least in part by augmenting CXCR2 ligand production by the tumor cells, an effect apparent in vivo and in the absence of PMNs themselves. These observations are consistent with our prior data correlating the onset and spatial distribution of hypoxia in PRPL tumors with the onset of PMN recruitment and their localized aggregation within the tumor, respectively, as well as with our prior observation that hypoxia induces the expression of IL-8, a human PMN chemoattractant, in cultured human endometrial carcinoma cells (5). Interestingly, we also found that hypoxia induces STAT3 phosphorylation in

PRPL tumor cells in vivo, and that STAT3 is necessary for CXCL5 expression and PMN recruitment, but the exact pathway that connects hypoxia to CXCL5 expression remains unclear. Similarly unclear is whether hypoxia is the sole STAT3 activator in PRPL lesions. As this seems unlikely given the many pathways that feed into STAT3, it is reasonable to assume that these other pathways also contribute to PMN recruitment to PRPL uteri.

Our data suggested that relief of tumor hypoxia inhibited PRPL tumor growth at least in part by limiting the ability of NE to induce tumor cell proliferation. In previous work on lung cancer, this pro-proliferative effect was ascribed to NE uptake by tumor cells and consequent modulation of mitogenic signaling pathways (14), but whether a similar mechanism applies here remains to be determined. Since *Elane* transcripts were undetectable in tumor-associated PMNs, however, the limiting effect of hyperoxia housing must have had post-transcriptional causes. Consistent with the results of our casein zymograms, one possibility is that the hyperoxia-induced reduction in uterine PMN densities meant that there were fewer cells available to release NE; a second is increased intrauterine expression of a NE inhibitor. It is also possible that the hyperoxia-induced redistribution of PMNs away from the tumor epithelium reduced tumor cell exposure to NE. The amelioration of tumor hypoxia might also have limited NE release from PMNs, consistent with the observed reduction in NE release from HIF-1α-deficient murine PMNs (24) and the ability of hypoxia, conversely, to promote NE release from human PMNs (22). Interestingly, our observations using pimonidazole as a hypoxia detection reagent also implicates NE in generating severe tumor hypoxia. We speculate that this effect might be the consequence of the ability of NE to cause vascular injury (48), which might generate focal areas of ischemia superimposed over the background levels of hypoxia that arise from the metabolic demands of the dividing tumor cells. These observations also raise the question of how frequently other kinds of tumors might show discrepant measurements of HIF-1α activation versus pimonidazole reactivity.

Relief of tumor hypoxia also inhibited tumor growth by promoting PMN-induced tumor cell death. This component of the response was associated with increased tumor cell sloughing and appeared to be mediated by the combined activities of MMP-9 and NOX2-derived ROS. Moreover, our gelatin zymograms indicated that PMNs were the primary source of MMP-9 in PRPL tumors as well as the primary cell type responsible for increased MMP-9 activation under hyperoxia housing conditions, while our RNA-Seq analysis linked increased MMP-9 activation to increased PMN expression of MMP-2 and MMP-14. Similarly, our flow cytometric analysis revealed that PMNs were by far the major ROS producers in PRPL tumors and that hyperoxia housing increased ROS

17

production by PMNs on a per cell basis and in a NOX2-dependent fashion. This increase paralleled the cells' increased expression of *Cybb* mRNA. These latter observations are consistent with the previously described ability of hypoxia, conversely, to inhibit *Cybb* expression and respiratory burst activity in isolated mouse PMN-MDSCs (26) and to inhibit respiratory burst activity in human PMNs (25). Together, these data thus suggest that hyperoxia housing increased the net exposure of the tumor epithelium to active MMP-9 and NOX2-derived ROS, both generated primarily by PMNs, even while it reduced uterine PMN densities and redistributed the cells away from the tumor epithelium. Despite evidence that PMN-derived ROS can directly kill tumor cells in vitro (17, 49), our previous finding that the cellular debris within the uterine lumen of PRPL mice contains many live tumor cells makes us suspect that the primary mechanism of tumor cell death is basement membrane degradation leading to tumor cell detachment from the endometrial stroma. Indeed, basement membrane degradation is another in vitro effect of ROS (50, 51), while MMP-9 can also degrade basement membranes in vitro and promotes epithelial cell detachment from basement membranes in the context of bullous pemphigoid disease in vivo (12, 13, 15). Moreover, basement membrane degradation is consistent with our ability to discern PMN-induced tumor cell sloughing via NOX2-derived ROS over a high background of PMN-derived mitochondrial ROS, as $H_2O_2$ generated by NOX2 but not by mitochondria has the capacity to be converted by granule-associated myeloperoxidase into hypochlorous acid, which is particularly degradative for ECM molecules (52). Basement membrane degradation is also consistent with the loss of $\alpha6\beta4$ polarization from the tumor cell basolateral surface, particularly given our prior observation that tumor cells from PRPL and PRPL-*Csf3r*^{-/-} mice express the same levels of total surface $\alpha6\beta4$ (5). NOX2-derived ROS also appeared to promote tumor cell proliferation, with the similar degree of reduction in tumor cell proliferation seen in PRPL-*Cybb*^{-/-} and PRPL-*Elane*^{-/-} mice suggesting an interaction between such ROS and NE. Indeed, previous work suggests that respiratory burst activity is required for NE release from azurophilic granules, at least in the context of NETosis (53).

Provocatively, improved tumor oxygenation also increased uterine PMN transcript levels of genes involved in peptide-MHC class II complex generation and co-stimulation, an effect confined to the CD11b^{hi} PMN subset. Given that these cells expressed high levels of ROS and so might be highly activated, it is unclear whether they themselves were transcriptionally altered by hyperoxia housing, or whether hyperoxia housing differentially promoted their survival within the uterus following their recruitment from the blood, where MHCII[+] PMNs were enriched in PRPL mice compared to non-

tumor-bearing controls. Either way, the existence of these MHCII$^+$ cells relate our findings to an emerging population of MHCII$^+$ PMNs with antigen presenting capacity previously identified in mice in the context of inflammation (54) and in human lung cancer specimens (9). Interestingly, hypoxic culture conditions were shown to prevent the generation of such "TAN hybrids" from human precursors in vitro, an observation that was used to explain why these cells were less prevalent in larger (i.e. more hypoxic) tumors in vivo (9). Similarly, the expression of SiglecF by PRPL tumor-associated PMNs relate our findings to the SiglecF$^{hi}$ PMNs recently described to populate murine models of lung cancer and that are thought to have tumor-promoting properties (8). Intriguingly, PMNs in the tumors of 4-wk old PRPL mice expressed much lower levels of SiglecF, on average, than the PMNs in these lung tumors, and only strongly upregulated SiglecF at more advanced stages of tumor development. Moreover, hyperoxia housing reduced SiglecF expression in 4-wk PRPL tumors as it increased the tumor-killing potential of the cells. These observations further suggest the potential of using SiglecF expression as a marker of tumor-promoting PMNs and raise questions about its potential causative role in fostering such pro-tumor functions.

Importantly, the effects of hypoxia on tumor-associated PMN behavior and phenotypes likely reflect the complex outcome of both PMN-intrinsic and -extrinsic pathways. For example, PMN accumulation in PRPL tumors was at least in part an indirect effect of tumor hypoxia, as it appeared mediated by STAT3-dependent production of CXCL5 (and possibly CXCL1 and CXCL2) by tumor cells, which in turn induced PMN recruitment. However, it has also previously been shown that hypoxia can directly extend PMN lifespan through cell-intrinsic, HIF-1$\alpha$- and HIF-2$\alpha$-dependent pathways (21, 23). Similarly, altered PMN effector function under hypoxic conditions might reflect in part the direct effects of hypoxia on PMN degranulation and respiratory burst activity, as described above, but also its indirect effects as mediated through other cell types. For example, extracellular adenosine, which is generated in the hypoxic tumor microenvironment (55), can inhibit PMN respiratory burst activity (56). Further work will be necessary to determine the identity and relative importance of these intrinsic and extrinsic pathways over the control of tumor-associated PMN phenotypes.

Although the experiments performed here were motivated by our interest in how hypoxia controls tumor-associated PMNs, they also bear upon the question of how hypoxia influences solid tumor development more generally. Indeed, while tumor hypoxia is well known to have many effects on tumor cells and the tumor microenvironment (30, 57), it has been difficult to discern their relative

importance since it has been difficult to control tumor oxygenation as the sole experimental variable. Thus, it is striking that altered PMN-tumor cell interactions are by far the dominant means through which relief of tumor hypoxia, achieved via the administration of respiratory hyperoxia, affects PRPL tumor growth. This dominance might reflect the high density of PMNs in PRPL lesions (5), or it might reflect, in principle, a lack of effect of hypoxia on the vascularity or the tumor cell-intrinsic growth characteristics of PRPL tumors. Since the lesions of 4-wk old PRPL mice are still at a relatively early stage of development, the net tumor growth-opposing effects of PMNs we document here may also reflect the possibility that PMNs become more overtly "pro-tumor" only with advancing stages of tumor formation, a possibility suggested by recent work on other tumor models (4, 9, 11) and consistent with the cells' tumor stage-dependent expression level of SiglecF. Thus, with special consideration of tumor stage, these results suggest that greater attention to direct PMN-tumor cell interactions is warranted when considering the role of hypoxia in other kinds of cancers. Moreover, they inform the interpretation of recent studies suggesting that therapeutic relief of tumor hypoxia augments anti-tumor lymphocyte responses (32, 33), as these studies did not address the potential contribution of PMNs as direct anti-tumor effectors. Indeed, given our data here and previously (5) that PMNs can directly combat PRPL tumor formation independently of all lymphocytes and that this activity can be increased with improved oxygenation, it will be of interest to determine the extent to which this information might help with the development of hypoxia reduction as a therapeutic tool in other cancer settings.

**METHODS**

**Animals.** PRPL ($Pgr^{cre/+}$ $Pten^{lox/lox}$) mice on a C57BL/6 background were generated as previously described (5) from $Pgr^{cre}$ mice (58) (the gift of Francesco DeMayo, Baylor College of Medicine) and $Pten^{lox/lox}$ mice (The Jackson Laboratory, stock no. 006440, referred to here as PL mice). PRPL mice were intercrossed to additional C57BL/6-background strains, namely $Csf3r^{-/-}$, $Stat3^{lox/lox}$, $Elane^{-/-}$, $Cybb^{-/-}$ (The Jackson Laboratory, stocks nos. 017838, 016923, 006112 and 002365, respectively) and $Mmp9^{-/-}$ mice (59) (the gift of Zena Werb, UCSF). The mice were maintained in specific pathogen-free animal barrier facilities at UCSF (all experiments aside from those on PRPL-$Stat3^{d/d}$ mice) and the NYU School of Medicine (PRPL-$Stat3^{d/d}$ mice).

**Treatments.** For hyperoxia studies, PRPL mice were housed in a Small A-Chamber environmental chamber with ProOx P110 oxygen controller (BioSpherix) set at 60% oxygen but otherwise the ambient humidity and temperature of our mouse holding room. For T cell depletion, mice were injected i.p. with anti-CD4 antibodies (300 µg, BioXCell; clone GK1.5) and anti-CD8 antibodies (200 µg, BioXCell; clone 2.43) on P18, P21, P24, and P27. For LPS stimulation, PL female mice were injected transcervically 24 h before sacrifice on P28 with 1.25 µg/g LPS from *Salmonella enterica* (serotype typhimurium, Sigma-Aldrich) dissolved in 10 µl PBS. Transcervical injection was performed as described (60). For the in situ detection of severe tumor hypoxia, mice were injected i.p. with 0.75 mg pimonidazole hydrochloride (Hypoxyprobe) 1.5 h prior to sacrifice.

**Flow cytometry**. Dissected whole uteri were weighed and digested as previously described (60). Briefly, minced uteri were incubated in Hank's Balanced Salt Solution containing 0.28 Wünsch units/ml Liberase TM Research Grade (Roche Life Science) and 30 µg/ml DNAase I (Roche) for 30 min at 37°C with intermittent trituration. Tissues were then washed, resuspended in PBS/1% FBS/5 mM EDTA, incubated at 37°C for an additional 15 min, then filtered through 40 µm nylon mesh. We RBC-lysed blood samples using Gey's buffer.

The following flow cytometry antibodies were from BioLegend: CD8α (clone 53–6.7), CD45 (30F-11), CD11c (N418), Ly6G (1A8), Ly6C (HK1.4), MHCII (I-A/I-E) (M5/114.15.2), F4/80 (BM8), EpCAM (CD326) (G8.8), ICAM2 (CD102) (3C4 (MIC2/4)), NK1.1 (PK136), Thy1.1 (53-2.1), rat IgG2b, and κ isotype control (RTK4530) (for MHCII staining). Antibodies to CD11b

(M1/70), SiglecF (E50-2440), TCRγδ (GL3), TCRβ (H57-597), rat IgG2a, κ isotype control (R35-95) (for SiglecF staining) were from BD Pharmingen. Antibodies to CD4 (RM4-5) were from Tonbo Biosciences. The cells were first incubated with rat anti-mouse CD16/CD32 (BioXCell; clone 2.4G2; 5 μg/ml for $10^6$ cells) to block non-specific antibody binding. Live/dead discrimination employed 5 μg/ml 7-aminoactinomycin D (BD Pharmingen) or Fixable Viability Dye eFluor 506 (Invitrogen). Samples were analyzed using a 18-color 4-laser BD LSRFortessa[TM] cytometer or sorted on a 18-color 4-laser BD ARIA2. CountBright beads (Invitrogen) were added to each sample to allow for leukocyte subset densities calculations (cells/mg tissue). For ROS production, digested cell preparations, prior to antibody staining, were cultured at $5.0 \times 10^5$ cells/ml in RPMI/10% FBS for 30 min at 37°C in a 5% $CO_2$ incubator in the presence of 12.5 ng/ml dihydrorhodamine 123 (Life Technologies) or vehicle control (0.025% DMSO). Flow cytometric analysis employed FlowJo (Tree Star).

**Immunofluorescence staining**. Immunofluorescence staining of paraformaldehyde-fixed, paraffin embedded tissue was performed as previously described (61). Depending upon the primary antibody, tissue sections were subjected to antigen retrieval either by incubation in 1 mg/ml trypsin in $H_2O$ for 11 min at 37°C, or by boiling in 0.01 M citric acid pH 6.0 (citrate) or 0.010 M Tris-EDTA pH 9.0 (TE) for 28 min in a pressure cooker. Slides were then blocked in PBS/3% bovine serum albumin (BSA; Sigma-Aldrich)/3% donkey serum (Millipore)/0.4% Triton X-100 (Sigma- Aldrich) for 1 h at RT, and then incubated overnight at 4°C with primary antibodies diluted in PBS/1% BSA/0.4% Triton X-100. Antibodies, antibody dilutions, and antigen retrieval methods were as follows: CXCL5 (1:100, trypsin; Lifespan Biosciences, rabbit polyclonal, Cat. #LS-C212192), Ly6G (1:100, citrate or TE; BD Pharmingen, rat monoclonal, clone 1A8), integrin α6 (1:1000, TE; Abcam, rabbit monoclonal, clone EPR18124), histone H3 phospho-Ser10 (1:100, citrate; Cell Signaling Technology, rabbit polyclonal, Cat. #9701), STAT3 phospho-Tyr705 (1:300, citrate; Cell Signaling Technology, rabbit polyclonal, Cat. #9131), HIF-1α (1:1000, TE; Novus Biologicals, rabbit polyclonal, Cat. #NB100-479B), NF-κB p65 phospho-Ser276 (1:3000, citrate; Abcam, rabbit polyclonal, Cat. #ab106129), CK8 (1:100, trypsin, citrate, or TE; University of Iowa, Developmental Studies Hybridoma Bank, rat monoclonal, clone TROMA-I), E-cadherin (1:1000, citrate or TE; Cell Signaling Technology, rabbit monoclonal, clone 24E10), cleaved caspase-3 (CC-3; 1:100, citrate; Cell Signaling Technology, rabbit polyclonal, Cat. #9661), pimonidazole (1:100, citrate; Hypoxyprobe, FITC-conjugated mouse monoclonal, clone

4.3.11.3), CD45 (1:100, citrate; BioLegend, rat monoclonal, clone I3/2.3), and TROP-2 (1:50, citrate; R&D Systems, goat polyclonal, Cat. #AF1122).

After incubation with primary antibodies, the sections were incubated for 30 min at RT in the following secondary antibodies from Jackson ImmunoResearch: donkey anti-rat IgG-Alexa Fluor 488 (CK8 and Ly6G) or -Alexa Fluor 594 (integrin α6), donkey anti-goat IgG-Alexa Fluor 647 (TROP-2), donkey anti-rabbit IgG-horseradish peroxidase (HRP; E-cadherin, pH3, CXCL5, pSTAT3, HIF1α, and NF-κB p65), or donkey anti-rat IgG-HRP (CD45). Secondary antibodies were diluted 1:200 either in PBS/1% BSA/0.4% Triton X-100 or, for HRP-conjugated antibodies, in TNB blocking buffer (PerkinElmer). HRP-labeled slides were subjected to tyramide signal amplification in PBS/1.8 μg/ml biotin-tyramide/0.0015% $H_2O_2$ for 5 min at RT, and then incubated 30 min at RT with 5 μg/ml streptavidin-Alexa Fluor 594 or -Alexa Fluor 488 (Life Technologies) diluted in 1% BSA. All slides were mounted using 4',6'-diamidino-2-phenylindole (DAPI)-containing Fluoromount-G (Electron Microscopy Sciences).

**Image acquisition, manipulation and analysis.** All immunofluorescent images were captured using an AxioImager M2 and Zen software (Zeiss). Panoramic views were generated by tiling images taken with the 10X objective.  For each primary antibody not revealing a structural feature of the tissue (i.e. antibodies towards CXCL5, pSTAT3, HIF-1α, NF-κB p65, integrin α6, Ly6G, pimonidazole, CC-3), images were respectively captured on the relevant fluorescent channel with the same exposure time and then subjected to the identical set of manipulations in Adobe Photoshop. Specifically, we first used the curves command to remove background fluorescence, and then the brightness/contrast command to achieve optimal visual discrimination across the set of images. For CK8, E-cadherin, TROP-2, CD45 and DAPI staining, brightness and contrast was optimized individually for each image. pH3 staining was binary and thus unaffected by modest image manipulations. In order to improve the publication quality of panoramic images, we applied the maximum filter of ImageJ (NIH, https://imagej.nih.gov/ij/) for some stains and blurred the DAPI counterstain.

Our tumor burden calculations employed E-cadherin staining and a histomorphometric determination of intact cross-sectional tumor area. For this latter determination, as well as the determination of the amount of sloughed tumor cells, we first used the threshold command of ImageJ to highlight and then calculate the total area of all E-cadherin[+] staining (i.e. intact plus sloughed tumor area, determined for 3-5 cross-sections per mouse). We then repeated this procedure after first deleting

regions of sloughed tumor, which were easily identified by eye because they were located within the lumen and had a macerated appearance, to determine the intact tumor area. For each cross-section, sloughed area was then calculated as (total area)-(intact area), and % sloughed area was calculated as (sloughed area)/(total area), and then averaged over all cross-sections analyzed for a given mouse. The % intact tumor area per total area of the cross-section was also calculated, and this value's average over all cross-sections analyzed for a mouse was then multiplied with the mouse's uterine weight to determine its tumor burden.

We used E-cadherin-stained sections and standard grid-based morphometry (62) to determine the amount of denuded endometrial surface. Specifically, % denuded surface was calculated as the number of times the grid intersected with a direct interface between the endometrial stroma and the uterine lumen (i.e. an interface with no covering epithelium), divided by the number of times the grid intersected with any kind of interface between uterine tissue and lumen (i.e. with or without a covering epithelium). Using a CK8 co-stain to identify the entire tumor epithelium, we similarly determined the percentage of basolateral tumor surface positive for $\alpha6$ integrin staining. For both calculations, at least three entire cross-sections were analyzed per mouse and then averaged.

For the CXCL5 quantification, we first used the CK8 co-stain and the Photoshop magic wand tool to identify all areas occupied by the tumor epithelium, and then ImageJ to apply a uniform threshold across all images in order to binarize the CXCL5 staining. The percentage of CXCL5^{+} tumor area was then calculated as the number of pixels positive for CXCL5 divided by the total number of pixels overlying tumor cells. An identical method was used to quantify pimonidazole staining, except that E-cadherin was used as the co-stain. The percentage of tumor cell nuclei staining positive for HIF-1$\alpha$, pSTAT3, or NF-$\kappa$B p65 was similarly calculated, however the CK8 and DAPI counterstains were together used to create a mask over all tumor cell nuclei. Determining the percentage of CC-3^{+} tumor cells again took a similar approach, since the extensive overlap between the CC-3 and DAPI staining allowed us to use the percentage of CC-3^{+} tumor cell nuclear area as a measure of the percentage of positive tumor cells. This analysis employed TROP-2/DAPI staining to create the tumor cell nuclear mask and the CD45 co-stain to exclude leukocytes. Percentages of PMNs within the tumor epithelium were quantified histologically by binarizing Ly6G-stained images and then calculating the percentage of positive pixels within or without an epithelial mask defined by the E-cadherin co-stain. For all these analyses, at least three entire cross-sections were analyzed per mouse and then averaged.  For the determination of % pH3^{+} tumor cells, which were rare, we hand-counted pH3^{+} tumor cells and total

DAPI[+] tumor cell nuclei over 3-5 10X images per mouse, identifying tumor cell areas by CK8 co-staining. At least 1500 total tumor cells were scored per mouse.

**RNA-seq**. PMNs (CD45^{+} Ly6G^{hi} CD11b^{+} cells) from disaggregated uteri (3 independent samples per group) were sorted on a 18-color 4-laser BD ARIA2. RNA was then isolated using an RNeasy Micro Kit (Qiagen). The samples were then processed by the UCSF Functional Genomics Core as follows: after a quality control test, a single-end 50 bp RNAseq library (Ovation/NexteraXT kit, Illumina®) was prepared, followed by sequencing on a Illumina HiSeq 4000 system (Illumina®). Sequencing provided 372 million total reads for the 6 samples with an average of 81.9% of these reads aligning uniquely to the mouse genome (Ensembl Mouse GRCm38.78). Alignment was performed using the Splice-aware STAR aligner STAR_2.4.2a (63). Reads uniquely mapped to known mRNAs were used to identify genes with differential expression (*FDR*<0.05) using the DESeq2 R package (64).

**Zymograms.** Lysates were prepared by homogenizing whole uterine tissue in RIPA buffer with Complete[TM] protease inhibitors (Thermo Scientific) using Lysing Matrix D tubes (MPBio) and an MPBio Homogenizer. For MMP-9 activity, 10 μg protein from each sample was loaded onto gelatin-containing 10% SDS-PAGE gels (Novex zymograms, Life Technology). For elastase activity, we used homemade 12% gels containing 1 mg/ml β-Casein (Sigma-Aldrich). Following renaturation, enzyme activities were revealed by staining the gels with Brilliant Blue G (Sigma Aldrich) followed by destaining. Image capture, analysis and quantification were performed using Chemidoc system (Bio-Rad) and the quantification tools of the ImageLab software (Bio-Rad). For each experiment, we normalized each inactive MMP-9 or elastase band intensity to their respective average intensity from the 3-4 samples run on each gel from mice housed under normoxia condition.

**Data availability.** RNA-Seq data sets were deposited in the NCBI's Gene Expression Omnibus database (GEO GSE137431).

**Statistics.** Statistical analyses were performed in GraphPad Prism. *P*-values were determined using a two-tailed Mann-Whitney test. In cases of multiple comparisons, the data were first analyzed by the Kruskal-Wallis test, and then Mann-Whitney-derived *P*-values were corrected using the Bonferroni adjustment. Statistical significance was defined as *P*<0.05.

**Study approval.** All animal experiments were approved by the Institutional Animal Care and Use Committees (IACUC) of UCSF and the NYU School of Medicine and were conducted in accordance with the relevant regulatory standards.

## AUTHOR CONTRIBUTIONS

K.M., A.B., S.M., and A.C. performed experiments; K.M., A.B., and A.E. designed experiments; C.L. helped conceptualize the project; K.M. and A.E. analyzed the data and wrote the manuscript.

## ACKNOWLEDGMENTS

## CONFLICT OF INTEREST STATEMENT

The authors have declared that no conflicts of interest exist.

## LITERATURE CITED

1.      Coffelt SB, Wellenstein MD, and de Visser KE. Neutrophils in cancer: neutral no more. *Nat Rev Cancer.* 2016;16(7):431-46.

2.      Shaul ME, and Fridlender ZG. Tumour-associated neutrophils in patients with cancer. *Nature Reviews Clinical Oncology.* 2019.

3.      Vols S, Sionov RV, and Granot Z. Always Look On the Bright Side: Anti-Tumor Functions of Neutrophils. *Curr Pharm Des.* 2017;23(32):4862-92.

4.      Eruslanov EB, et al. Tumor-associated neutrophils stimulate T cell responses in early-stage human lung cancer. *J Clin Invest.* 2014;124(12):5466-80.

5.      Blaisdell A, et al. Neutrophils Oppose Uterine Epithelial Carcinogenesis via Debridement of Hypoxic Tumor Cells. *Cancer Cell.* 2015;28(6):785-99.

6.      Kiss M, Van Gassen S, Movahedi K, Saeys Y, and Laoui D. Myeloid cell heterogeneity in cancer: not a single cell alike. *Cell Immunol.* 2018;330:188-201.

7.      Fridlender ZG, et al. Polarization of tumor-associated neutrophil phenotype by TGF-beta: "N1" versus "N2" TAN. *Cancer Cell.* 2009;16(3):183-94.

8.      Engblom C, et al. Osteoblasts remotely supply lung tumors with cancer-promoting SiglecF(high) neutrophils. *Science.* 2017;358(6367).

9.      Singhal S, et al. Origin and Role of a Subset of Tumor-Associated Neutrophils with Antigen-Presenting Cell Features in Early-Stage Human Lung Cancer. *Cancer Cell.* 2016;30(1):120-35.

10.     Finisguerra V, et al. MET is required for the recruitment of anti-tumoural neutrophils. *Nature.* 2015;522(7556):349-53.

11.     Mishalian I, Bayuh R, Levy L, Zolotarov L, Michaeli J, and Fridlender ZG. Tumor-associated neutrophils (TAN) develop pro-tumorigenic properties during tumor progression. *Cancer Immunol Immunother.* 2013;62(11):1745-56.

12.     Liu Z, et al. The serpin alpha1-proteinase inhibitor is a critical substrate for gelatinase B/MMP-9 in vivo. *Cell.* 2000;102(5):647-55.

13.     Liu Z, Li N, Diaz LA, Shipley M, Senior RM, and Werb Z. Synergy between a plasminogen cascade and MMP-9 in autoimmune disease. *J Clin Invest.* 2005;115(4):879-87.

14.     Houghton AM, et al. Neutrophil elastase-mediated degradation of IRS-1 accelerates lung tumor growth. *Nat Med.* 2010;16(2):219-23.

15.     Kessenbrock K, Plaks V, and Werb Z. Matrix metalloproteinases: regulators of the tumor microenvironment. *Cell.* 2010;141(1):52-67.

16.   Bao S, Carr ED, Xu YH, and Hunt NH. Gp91(phox) contributes to the development of experimental inflammatory bowel disease. *Immunology and cell biology.* 2011;89(8):853-60.

17.   Granot Z, Henke E, Comen EA, King TA, Norton L, and Benezra R. Tumor entrained neutrophils inhibit seeding in the premetastatic lung. *Cancer Cell.* 2011;20(3):300-14.

18.   Treffers LW, Hiemstra IH, Kuijpers TW, van den Berg TK, and Matlung HL. Neutrophils in cancer. *Immunol Rev.* 2016;273(1):312-28.

19.   Lodge KM, Thompson AA, Chilvers ER, and Condliffe AM. Hypoxic regulation of neutrophil function and consequences for Staphylococcus aureus infection. *Microbes Infect.* 2017;19(3):166-76.

20.   Lin N, and Simon MC. Hypoxia-inducible factors: key regulators of myeloid cells during inflammation. *J Clin Invest.* 2016;126(10):3661-71.

21.   Walmsley SR, et al. Hypoxia-induced neutrophil survival is mediated by HIF-1alpha-dependent NF-kappaB activity. *J Exp Med.* 2005;201(1):105-15.

22.   Hoenderdos K, et al. Hypoxia upregulates neutrophil degranulation and potential for tissue injury. *Thorax.* 2016;71(11):1030-8.

23.   Thompson AA, et al. Hypoxia-inducible factor 2alpha regulates key neutrophil functions in humans, mice, and zebrafish. *Blood.* 2014;123(3):366-76.

24.   Peyssonnaux C, et al. HIF-1alpha expression regulates the bactericidal capacity of phagocytes. *J Clin Invest.* 2005;115(7):1806-15.

25.   McGovern NN, et al. Hypoxia selectively inhibits respiratory burst activity and killing of Staphylococcus aureus in human neutrophils. *J Immunol.* 2011;186(1):453-63.

26.   Corzo CA, et al. HIF-1alpha regulates function and differentiation of myeloid-derived suppressor cells in the tumor microenvironment. *J Exp Med.* 2010;207(11):2439-53.

27.   Marvel D, and Gabrilovich DI. Myeloid-derived suppressor cells in the tumor microenvironment: expect the unexpected. *J Clin Invest.* 2015;125(9):3356-64.

28.   Walmsley SR, et al. Prolyl hydroxylase 3 (PHD3) is essential for hypoxic regulation of neutrophilic inflammation in humans and mice. *J Clin Invest.* 2011;121(3):1053-63.

29.   Cramer T, et al. HIF-1alpha is essential for myeloid cell-mediated inflammation. *Cell.* 2003;112(5):645-57.

30.   Chouaib S, Noman MZ, Kosmatopoulos K, and Curran MA. Hypoxic stress: obstacles and opportunities for innovative immunotherapy of cancer. *Oncogene.* 2017;36(4):439-45.

31.    Dewhirst MW, Mowery YM, Mitchell JB, Cherukuri MK, and Secomb TW. Rationale for hypoxia assessment and amelioration for precision therapy and immunotherapy studies. *J Clin Invest.* 2019;129(2):489-91.

32.    Hatfield SM, et al. Immunological mechanisms of the antitumor effects of supplemental oxygenation. *Sci Transl Med.* 2015;7(277):277ra30.

33.    Jayaprakash P, et al. Targeted hypoxia reduction restores T cell infiltration and sensitizes prostate cancer to immunotherapy. *J Clin Invest.* 2018;128(11):5137-49.

34.    Di Cristofano A, and Ellenson LH. Endometrial carcinoma. *Annu Rev Pathol.* 2007;2:57-85.

35.    Daikoku T, et al. Conditional loss of uterine Pten unfailingly and rapidly induces endometrial cancer in mice. *Cancer Res.* 2008;68(14):5619-27.

36.    Tibbles PM, and Edelsberg JS. Hyperbaric-oxygen therapy. *N Engl J Med.* 1996;334(25):1642-8.

37.    Maybin JA, Murray AA, Saunders PTK, Hirani N, Carmeliet P, and Critchley HOD. Hypoxia and hypoxia inducible factor-1alpha are required for normal endometrial repair during menstruation. *Nature communications.* 2018;9(1):295.

38.    Kallet RH, and Matthay MA. Hyperoxic acute lung injury. *Respir Care.* 2013;58(1):123-41.

39.    Kim MH, Yang D, Kim M, Kim SY, Kim D, and Kang SJ. A late-lineage murine neutrophil precursor population exhibits dynamic changes during demand-adapted granulopoiesis. *Sci Rep.* 2017;7:39804.

40.    Campbell EL, et al. Transmigrating neutrophils shape the mucosal microenvironment through localized oxygen depletion to influence resolution of inflammation. *Immunity.* 2014;40(1):66-77.

41.    Gross MW, Karbach U, Groebe K, Franko AJ, and Mueller-Klieser W. Calibration of misonidazole labeling by simultaneous measurement of oxygen tension and labeling density in multicellular spheroids. *Int J Cancer.* 1995;61(4):567-73.

42.    Jiang BH, Semenza GL, Bauer C, and Marti HH. Hypoxia-inducible factor 1 levels vary exponentially over a physiologically relevant range of O2 tension. *Am J Physiol.* 1996;271(4 Pt 1):C1172-80.

43.    Vandooren J, Van den Steen PE, and Opdenakker G. Biochemistry and molecular biology of gelatinase B or matrix metalloproteinase-9 (MMP-9): the next decade. *Crit Rev Biochem Mol Biol.* 2013;48(3):222-72.

44.    Borregaard N, and Cowland JB. Granules of the human neutrophilic polymorphonuclear leukocyte. *Blood.* 1997;89(10):3503-21.

45. Shaul ME, et al. Tumor-associated neutrophils display a distinct N1 profile following TGFbeta modulation: A transcriptomics analysis of pro- vs. antitumor TANs. *Oncoimmunology.* 2016;5(11):e1232221.

46. Condamine T, et al. Lectin-type oxidized LDL receptor-1 distinguishes population of human polymorphonuclear myeloid-derived suppressor cells in cancer patients. *Sci Immunol.* 2016;1(2).

47. Sundqvist M, et al. Elevated Mitochondrial Reactive Oxygen Species and Cellular Redox Imbalance in Human NADPH-Oxidase-Deficient Phagocytes. *Frontiers in immunology.* 2017;8:1828.

48. Hirahashi J, et al. Mac-1 signaling via Src-family and Syk kinases results in elastase-dependent thrombohemorrhagic vasculopathy. *Immunity.* 2006;25(2):271-83.

49. Clark RA, and Klebanoff SJ. Neutrophil-mediated tumor cell cytotoxicity: role of the peroxidase system. *J Exp Med.* 1975;141(6):1442-7.

50. Riedle B, and Kerjaschki D. Reactive oxygen species cause direct damage of Engelbreth-Holm-Swarm matrix. *Am J Pathol.* 1997;151(1):215-31.

51. Owen CA, and Campbell EJ. The cell biology of leukocyte-mediated proteolysis. *J Leukoc Biol.* 1999;65(2):137-50.

52. Woods AA, and Davies MJ. Fragmentation of extracellular matrix by hypochlorous acid. *Biochem J.* 2003;376(Pt 1):219-27.

53. Metzler KD, Goosmann C, Lubojemska A, Zychlinsky A, and Papayannopoulos V. A myeloperoxidase-containing complex regulates neutrophil elastase release and actin dynamics during NETosis. *Cell Rep.* 2014;8(3):883-96.

54. Geng S, et al. Emergence, origin, and function of neutrophil-dendritic cell hybrids in experimentally induced inflammatory lesions in mice. *Blood.* 2013;121(10):1690-700.

55. Hatfield SM, et al. Systemic oxygenation weakens the hypoxia and hypoxia inducible factor 1alpha-dependent and extracellular adenosine-mediated tumor protection. *J Mol Med (Berl).* 2014;92(12):1283-92.

56. Wang X, and Chen D. Purinergic Regulation of Neutrophil Function. *Frontiers in immunology.* 2018;9:399.

57. Petrova V, Annicchiarico-Petruzzelli M, Melino G, and Amelio I. The hypoxic tumour microenvironment. *Oncogenesis.* 2018;7(1):10.

58. Soyal SM, et al. Cre-mediated recombination in cell lineages that express the progesterone receptor. *Genesis.* 2005;41(2):58-66.

59.     Vu TH, et al. MMP-9/gelatinase B is a key regulator of growth plate angiogenesis and apoptosis of hypertrophic chondrocytes. *Cell.* 1998;93(3):411-22.

60.     Collins MK, Tay CS, and Erlebacher A. Dendritic cell entrapment within the pregnant uterus inhibits immune surveillance of the maternal/fetal interface in mice. *J Clin Invest.* 2009;119(7):2062-73.

61.     Blaisdell A, and Erlebacher A. In: Croy BA, Yamada AT, DeMayo FJ, and Adamson SL eds. *The Guide to Investigation of Mouse Pregnancy.* Boston: Academic Press; 2014:577-89.

62.     Weibel ER. Stereological principles for morphometry in electron microscopic cytology. *International review of cytology.* 1969;26:235-302.

63.     Dobin A, et al. STAR: ultrafast universal RNA-seq aligner. *Bioinformatics.* 2013;29(1):15-21.

64.     Love MI, Huber W, and Anders S. Moderated estimation of fold change and dispersion for RNA-seq data with DESeq2. *Genome Biol.* 2014;15(12):550.
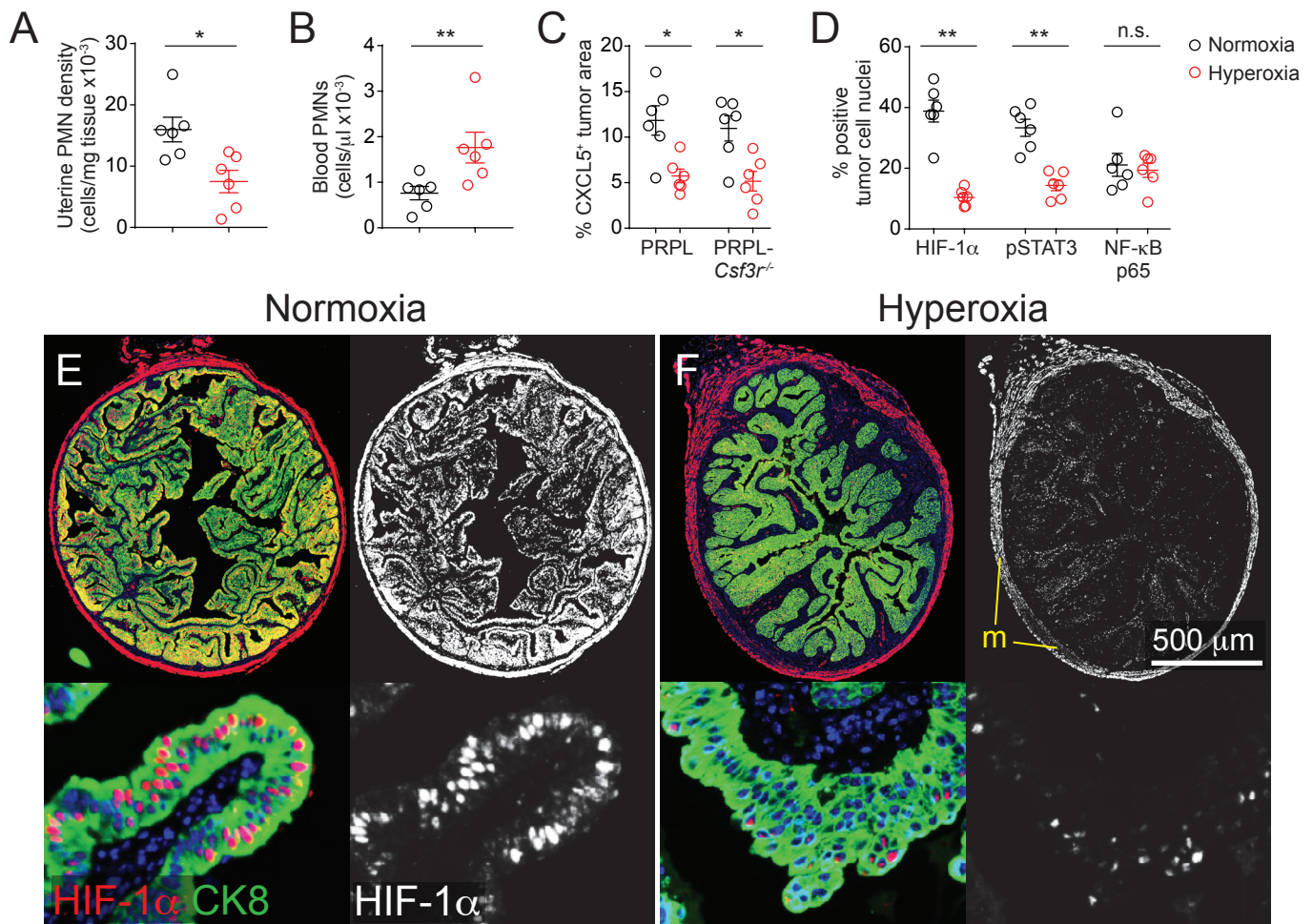
Figure 1. Improved tumor oxygenation reduces PMN recruitment to PRPL tumors. Mice were housed in either ambient $O_2$ (normoxia conditions) or 60% $O_2$ (hyperoxia conditions) for the last 10 days prior to sacrifice on P28. (A, B) Uterine PMN densities and blood PMN concentrations in PRPL mice, as determined by flow cytometry. Uteri were enzymatically disaggregated prior to analysis. PMNs were identified as CD45$^+$ Ly6G$^{hi}$ cells (see Supplemental Figure 1D for gating). (C) Quantification of CXCL5 expression by tumor cells. The cross-sectional area of tumor cells expressing CXCL5 was determined by immunofluorescence staining of uterine tissue sections and normalized to the cross-sectional area of all tumor cells, as identified by cytokeratin 8 (CK8) co-staining. See Supplemental Figure 2A-D for representative images. (D) Quantification of nuclear HIF-1$\alpha$, phospho-STAT3 (pSTAT3) and NF-$\kappa$B p65 expression by tumor cells in PRPL-*Csf3r$^{-/-}$* mice, as determined by immunofluorescence staining. The area of positive staining overlying tumor cell nuclei was normalized to the total tumor cell nuclear area per section. (E, F) Representative HIF-$\alpha$/CK8-stained sections of PPRL-*Csf3r$^{-/-}$* mice, with close-ups (lower panels) (*n*=6 mice/group; DAPI counterstain). The staining in the myometrium (m) appeared artifactual as it was not cell-associated. Graphs also show mean±SEM; *, *P*<0.05; **, *P*<0.01 by two-tailed Mann-Whitney *U* test; n.s., not significant.
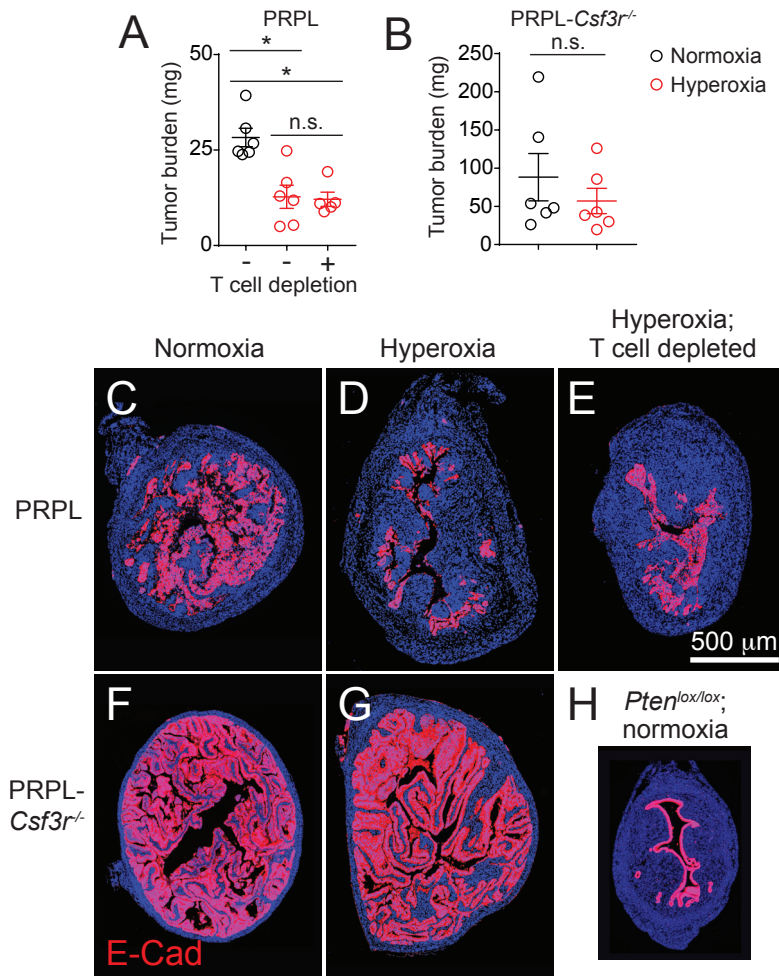
**Figure 2. Relief of tumor hypoxia improves net PMN-dependent tumor control.** (A, B) Tumor burden, calculated as the product of uterine weight and percent cross-sectional area of uterus comprised of tumor cells (Supplemental Figure 4A-B shows these values). Tumor cells were identified by E-cadherin (E-Cad) immunostaining. The mice were sacrificed on P28; T cells were depleted by administering anti-CD4 and anti-CD8 antibodies on P18, P21, P24, and P27. (C, H) Representative E-Cad-stained sections (*n*=6 mice/group; DAPI counterstain). Panel H shows, to scale, a section from a non-tumor-bearing control *Pten^{lox/lox}* ("PL") mouse on P28 as an additional point of comparison. Graphs also show mean±SEM; *, *P*<0.05 by two-tailed Mann-Whitney *U* test. Panel A was first assessed by the Kruskal-Wallis test (*P*<0.01) and *P*-values were Bonferroni-adjusted for multiple comparisons.
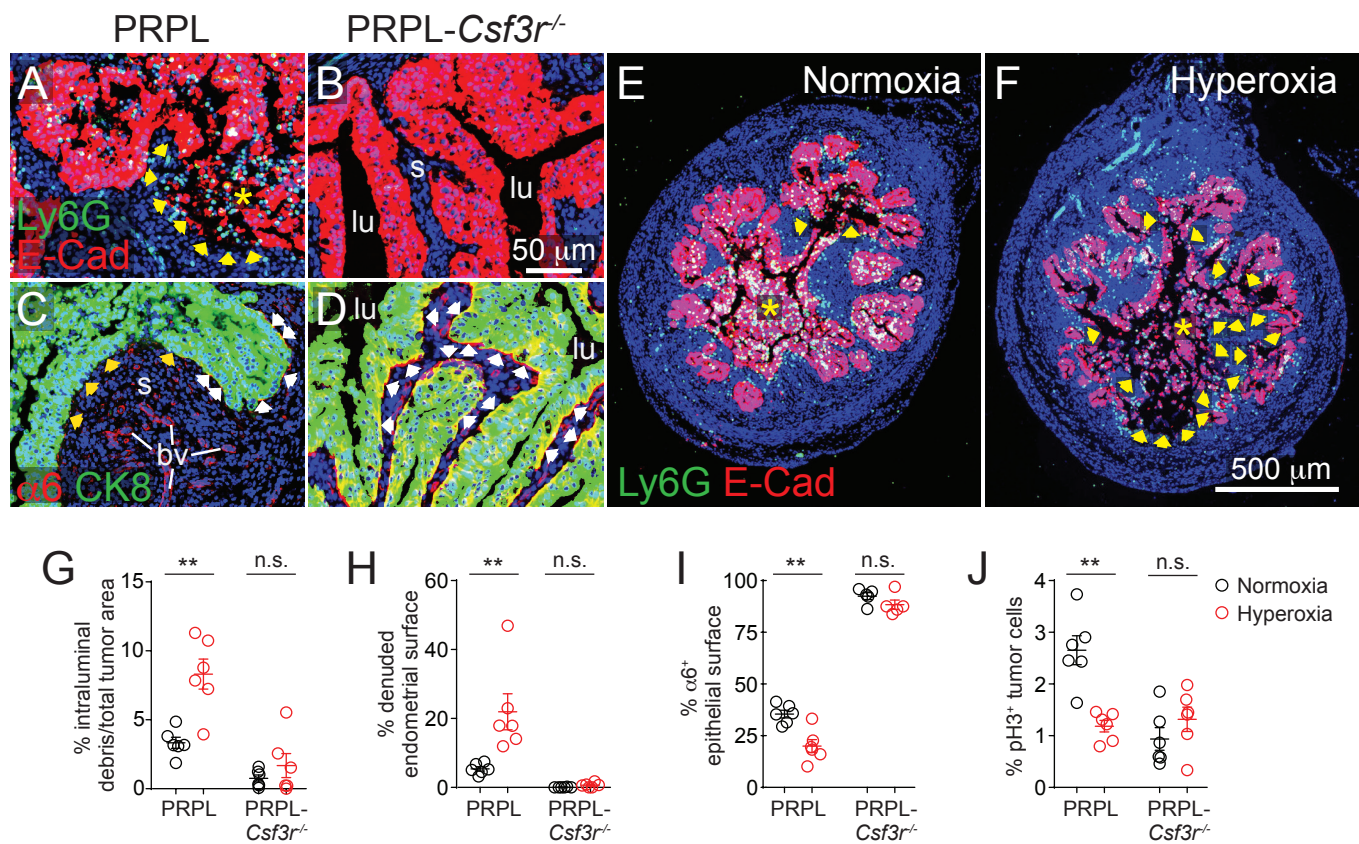
**Figure 3. PMNs simultaneously promote and inhibit PRPL tumor growth, with the two effects divergently influenced by tumor hypoxia.** PRPL (A, C) and PRPL-*Csf3r⁻/⁻* (B, D) mice were sacrificed on P28. (A, B) E-Cad/Ly6G double immunostaining to illustrate PMN-dependent tumor cell sloughing and denudation of the uterine stroma (see also ref. (5)). Asterisks indicate intraluminal tumor cell debris admixed with PMNs. The arrows demarcate the nearby denuded endometrial surface. s, endometrial stroma; lu, uterine lumen. (C, D) α6/CK8 double immunostaining to illustrate PMN-dependent loss of α6 integrin from the basolateral tumor cell membrane (see also ref. (5)). In the PRPL mouse (C), note the epithelial/stromal interface completely devoid of 6 staining (yellow arrowheads) and the intermittent α6 staining at other locations along this interface (white arrowheads). Blood vessels (bv) remain α6⁺. In the PRPL-*Csf3r⁻/⁻* mouse (D), α6 staining is largely continuous along the epithelial/stromal interface (see Supplemental Figure 5A-D for additional representative images). (E, F) Representative E-Cad-stained uterine sections of PRPL mice housed under normoxia and hyperoxia conditions (*n*=6 mice/group) to illustrate sloughed tumor cells (asterisks) and denuded endometrial surfaces (arrows). (G, H) Tumor cell sloughing (percent intraluminal debris of total tumor area, G) and percentage of denuded endometrial surface (H), determined from E-Cad-stained sections. (I) Percentage of tumor epithelial surface with basolateral α6 integrin staining, determined from α6/CK8-stained sections. (J) Tumor cell proliferation, as measured by phospho-histone H3 (pH3) immunostaining to identify mitotic cells. Graphs also show mean±SEM. **, *P*<0.01 by two-tailed Mann-Whitney *U* test.
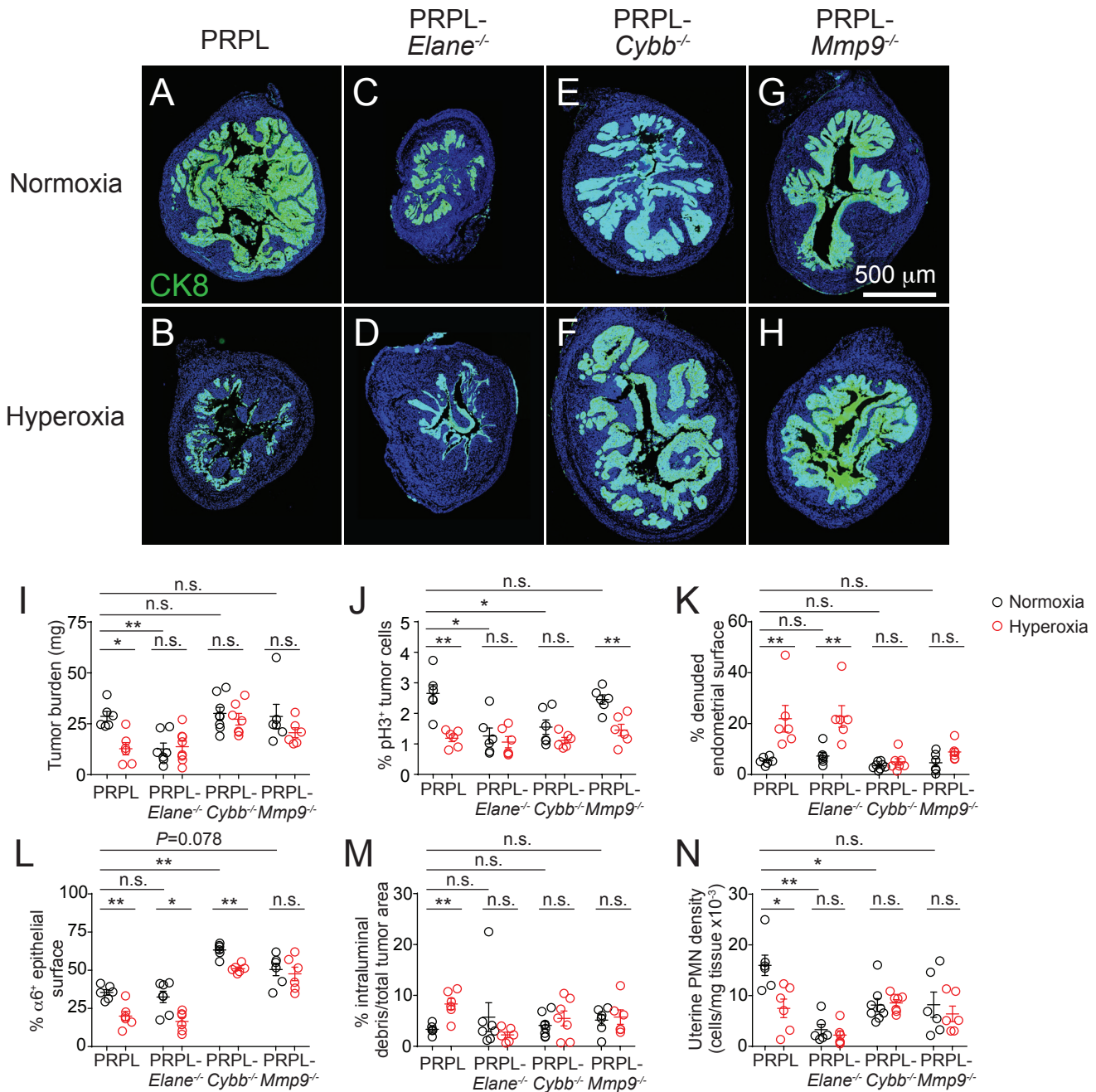
**Figure 4. Role of NE, neutrophil-derived ROS, and MMP-9 in PMN control over tumor cell death and proliferation.** (A-H) Representative CK8-stained sections of PRPL (A, B), PRPL-*Elane*^{-/-} (C, D), PRPL-*Cybb*^{-/-} (E, F) and PRPL-*Mmp9*^{-/-} (G, H) mice, housed in normoxia or hyperoxia conditions (*n*=6-8 mice/group). These are the same sections for which α6 co-staining is shown in Supplemental Figure 5. Quantification of (I) tumor burden, (J) tumor cell proliferation, (K) percentage of denuded endometrial surface, (L) percentage of tumor epithelial surface with basolateral α6 integrin staining, (M) percentage of sloughed tumor cells, and (N) uterine PMN tissue densities, as determined by flow cytometry. The data for PRPL mice are the same as in Figures 1-3. See Supplemental Figure 5 for representative images of α6 immunostaining. Graphs also show mean±SEM. *, *P*<0.05; **, *P*<0.01 by two-tailed Mann-Whitney *U* test. Differences between normoxia data were first assessed by the Kruskal-Wallis test (*P*<0.01) and *P*-values were Bonferroni-adjusted for multiple comparisons.
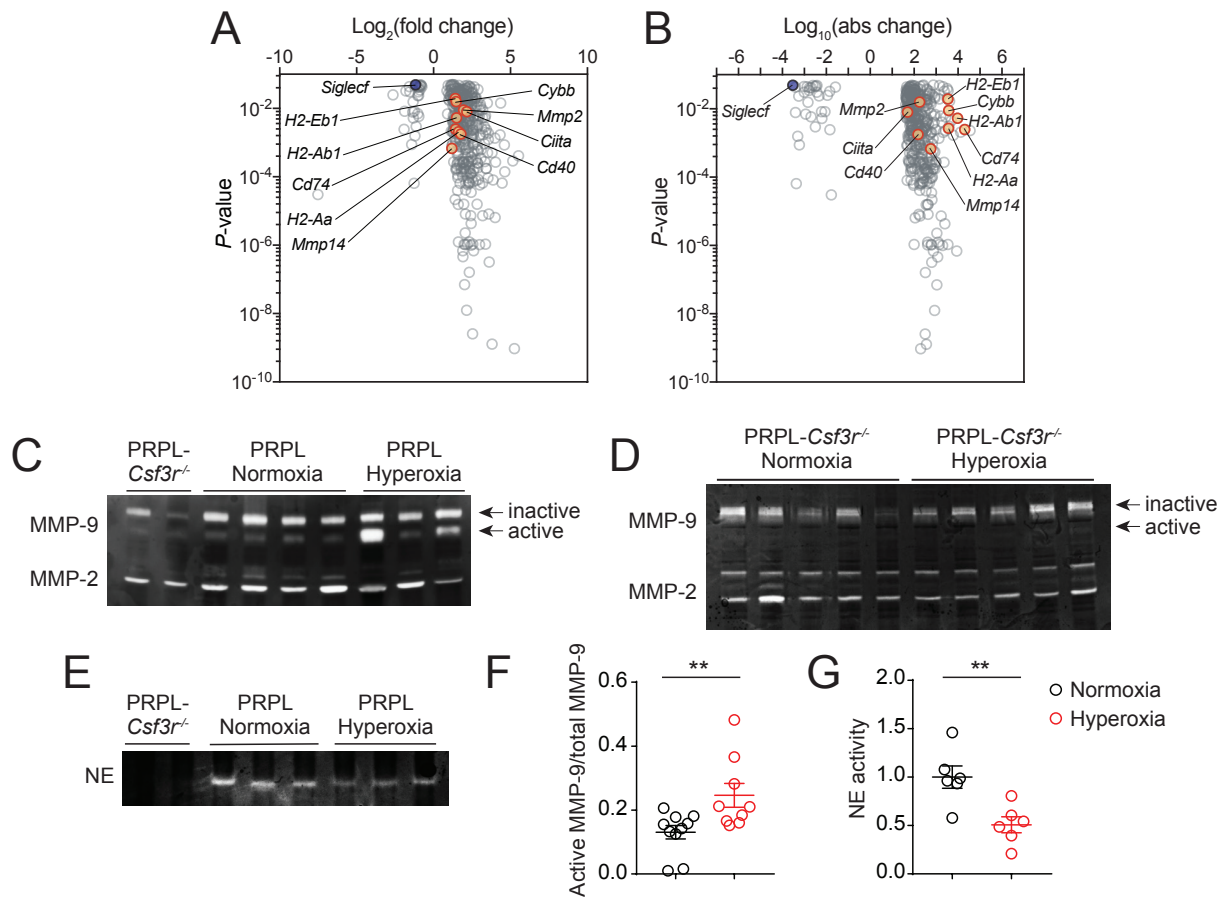
**Figure 5. Relief of tumor hypoxia alters the transcriptional signature of tumor-associated PMNs and their production of active MMP-9 and NE.** (A) Volcano plot showing the 423 differentially expressed protein-coding genes (*FDR*<0.05) in PMNs isolated from PRPL mice housed under normoxia versus hyperoxia conditions (*n*=3 per group). We excluded genes whose maximal average normalized reads in both of the two groups was less than 50. (B) Volcano plot of this same gene set but with the x-axis showing the $\log_{10}$ of the absolute difference in mean normalized reads, to accentuate genes that are more differentially expressed in absolute terms. (C-E) Gelatin and casein zymograms performed on uterine extracts. Each lane represents a different mouse. Equal protein amounts were loaded per well. (F, G) Quantification of MMP-9 and NE band intensities. Graphs also show mean±SEM. **, *P*<0.01 by two-tailed Mann-Whitney *U* test. In addition to the two gels shown (C and E), these data came from extracts run on two additional gelatin zymograms and one additional casein zymogram.
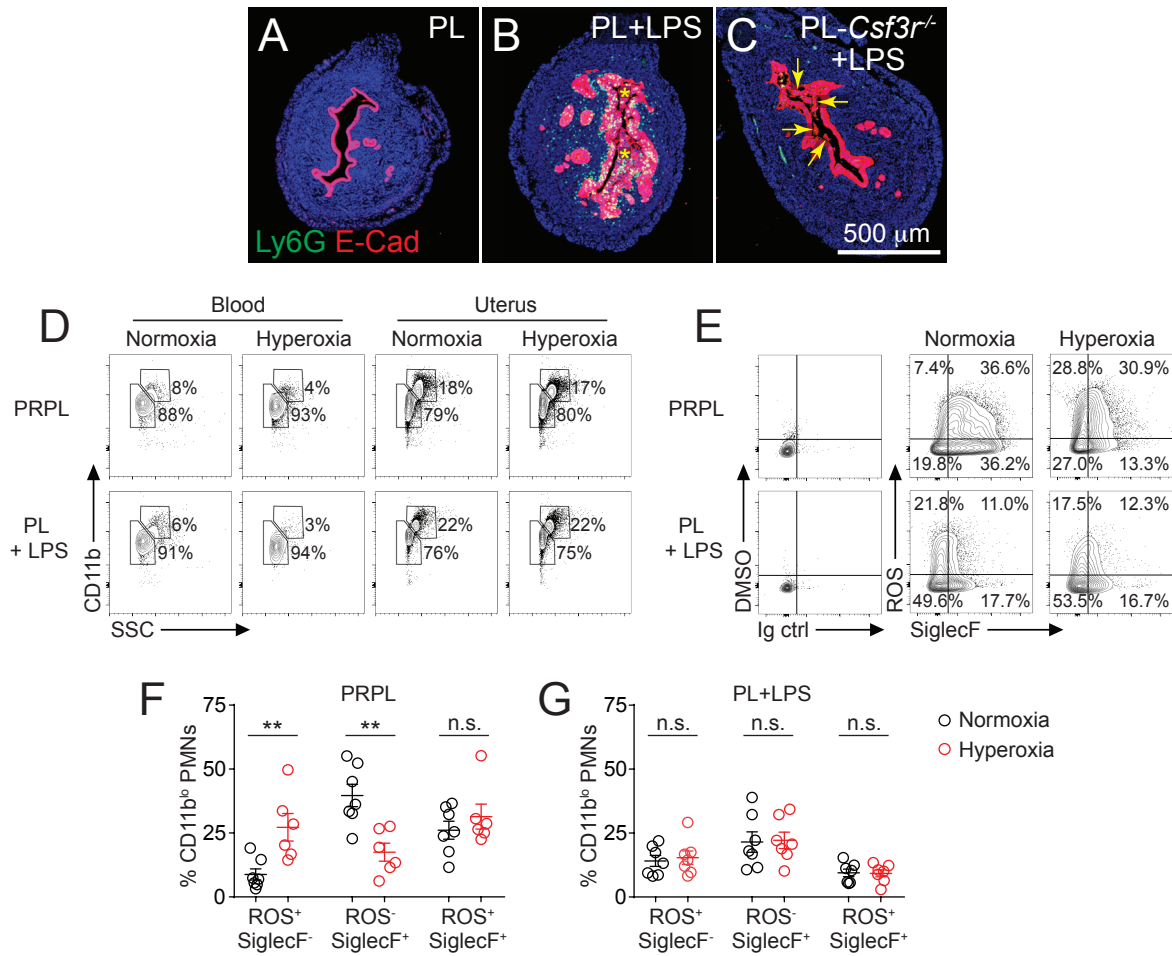
**Figure 6. Relief of tumor hypoxia alters the phenotype of tumor-associated PMNs.** PRPL mice were subjected to hyperoxia housing for 10 days prior to sacrifice on P28; PL and PL-*Csf3r⁻/⁻* mice received intrauterine injections of LPS 24 h prior to sacrifice on P28. Some of the PL mice were also subjected to hyperoxia housing for this 24 h period. (A-C) Representative E-cad-stained uterine cross-sections ($n$=5-8 mice/group). Asterisks (B) and arrows (C) indicate intraluminal debris; see Supplemental Figure 8A for its quantification. (D) Representative flow cytometry plots of Ly6G$^{hi}$ cells from the blood and uteri ($n$=6-7 mice/group, see Supplemental Figure 8B for quantification of uterine PMNs). (E) Representative flow cytometry plots showing ROS production and SiglecF expression by uterine CD11b$^{lo}$ PMNs ($n$=6-7 mice/group). ROS production was determined through use of dihydrorhodamine 123, a cell-permeable fluorescent ROS detection reagent. DMSO is the solvent for this reagent. (F, G) Flow cytometric quantification of ROS production and SiglecF expression by CD11b$^{lo}$ PMNs. Cells were gated on live/CD45$^{+}$/Ly6G$^{hi}$ events, and then were subdivided according to CD11b expression levels (see Supplemental Figure 8C-E for analysis of the CD11b$^{hi}$ cells). Graphs also show mean±SEM. **, $P$< 0.01 by two-tailed Mann-Whitney $U$ test.
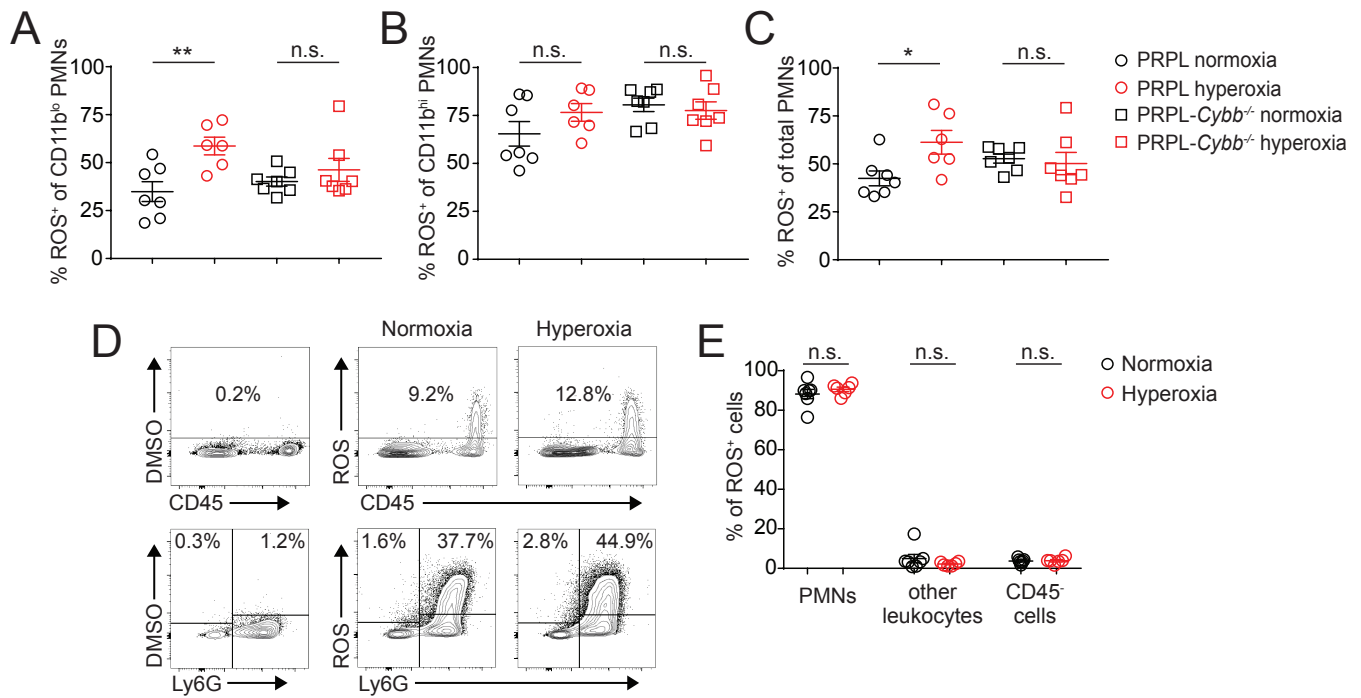
**Figure 7. Relief of tumor hypoxia increases NOX2-dependent ROS production by tumor-associated PMNs.** (A-C) Flow cytometric assessment of ROS production (using dihydrorhodamine 123) by the indicated PMN subsets. (D) Representative flow cytometry plots (*n*=6 mice/group) and (E) quantification of ROS production by all cell types within PRPL uteri. Graphs also show mean±SEM. *, *P*< 0.05; **, *P*< 0.01 by two-tailed Mann-Whitney *U* test.